Deterministic solvers to Boltzmann-Poisson Dynamics

An application to submicron semiconductor device model simulation

Irene M. Gamba
The University of Texas at Austin
ICES and Mathematics Department

In collaboration with

José A. Carrillo
ICREA - Department de Matemàtiques, Universitat Autònoma de Barcelona, Spain -

Armando Majorana
Dipartimento di Matematica e Informatica, Università di Catania, Catania, Italy

Chi Wang Shu
Brown University, Division of Applied Mathematics Department

Outline

- Introduction
  - Semiclassical model for charge particle transport
  - Change of variables: 1-D, 2-D, Si,
- Numerical method
  - WENO reconstruction
  - Numerical scheme: boundary conditions and properties
- Simulation
  - 1-D test case: n^+-n-n^+ diode
  - Comparisons to DSMC and deterministic simulations
  - 2-D devices: MESFET and MOSFET
  - Boundary singularities
  - Comparisons for BTE-Poisson - DSMC vs. WENO

References

- J.A. Carrilo, I.M. Gamba, A. Majorana, C.W. Shu [4, 7, 6]
- For MonteCarlo solvers A. Majorana, C. Millazo and O. Muscato[13], following [12]
- For motion in time data see: `http://kinetic.mat.uab.es/~carrillo/gallery1.html`

The Boltzmann-Poisson system for semiconductors [1]

$$\frac{\partial f}{\partial t} + \frac{1}{\hbar}\nabla_{\mathsf{k}}\varepsilon \cdot \nabla_{\mathsf{x}} f - \frac{e}{\hbar} E \cdot \nabla_{\mathsf{k}} f = Q(f) \qquad \text{BTE}$$

$$\Delta V = \frac{e}{\varepsilon_o}\left[\rho(t,\mathsf{x}) - C(\mathsf{x})\right], \qquad \text{Poisson Equation}$$

$$E(t,x) = -\nabla_x V \qquad \text{Electric force field,}$$

$$\rho(f)(t,x) = \int_{\mathbb{R}^3} f(t,x,\mathsf{k})d\mathsf{k}, \quad x \in \Omega,\ t \geq 0, \qquad \text{mass density,}$$

$$\varepsilon(\mathsf{k}) = \frac{1}{1+\sqrt{1+2\,\dfrac{\tilde{\alpha}}{m^*}\hbar^2\,|\mathsf{k}|^2}}\,\frac{\hbar^2}{m^*}\,|\mathsf{k}|^2 \qquad \text{Kane dispersion relation,}$$

m^* : effective mass $\qquad \tilde{\alpha}$: non − parabolicity factor

[1] Reggiani[17]

Collision operator [2]

$$Q(f)(t,\mathsf{x},\mathsf{k}) = \int_{\mathbb{R}^3} \left[S(\mathsf{k}',\mathsf{k})f(t,\mathsf{x},\mathsf{k}') - S(\mathsf{k},\mathsf{k}')f(t,\mathsf{x},\mathsf{k})\right]\, d\mathsf{k}'$$

Acoustic and optical non-polar phonon scattering:

$$S(\mathsf{k},\mathsf{k}') = K_0(\mathsf{k},\mathsf{k}')\delta(\varepsilon(\mathsf{k}') - \varepsilon(\mathsf{k})) +$$
$$K(\mathsf{k},\mathsf{k}')\left[(\mathsf{n}_q+1)\delta(\varepsilon(\mathsf{k}') - \varepsilon(\mathsf{k}) + \hbar\omega) + \mathsf{n}_q\delta(\varepsilon(\mathsf{k}') - \varepsilon(\mathsf{k}) - \hbar\omega)\right]$$

$$\mathsf{n}_q = \left[\exp\left(\frac{\hbar\omega}{k_B T_L}\right) - 1\right]^{-1} \quad \text{Occupation \# of phonons}$$

Si device: Scattering collision kernel constants

$$K = D_t k^2/(8\pi^2\rho_0\omega), \qquad D_t k : \text{Optical coupling constant}$$

$$K_0 = k_B T_L {E_{ac}}^2/(4\pi^2\hbar {u_l}^2\rho_0), \qquad E_{ac} : \text{deformation potential}$$

[2] Reggiani [17]; Jacoboni and Lugli [12];

Change of variables 1D [3]

After adimensionalization and changing to pseudo-cyllindrical coordinates:

$$\mathrm{k} = \sqrt{2}\frac{\sqrt{m^* k_B T_L}}{\hbar}\sqrt{w}\sqrt{1+\alpha_K w}\,(\sqrt{1-\mu^2}\cos\phi, \sqrt{1-\mu^2}\sin\phi, \mu)$$

we consider

$$\Phi(t,z,w,\mu) = s(w)F(t,z,w,\mu)$$

with

$$s(w) = \sqrt{w(1+\alpha_K w)}(1+2\alpha_K w)$$

that satisfies

$$\frac{\partial\Phi}{\partial t} + \frac{\partial}{\partial z}(a_1\Phi) + \frac{\partial}{\partial w}(a_2\Phi) + \frac{\partial}{\partial \mu}(a_3\Phi) = s(w)C(\Phi)$$

[3] Fatemi and Odeh[9]; Majorana and Pidatella[14]

Change of variables 1D [4]

Fluxes are:

$$a_1 = a_1(w, \mu) = \frac{1}{t_*} \frac{\mu s(w)}{(1 + 2\alpha_K w)^2},$$

$$a_2 = a_2(t, z, w, \mu) = -\frac{E(t, z)}{t_*} \frac{2\mu s(w)}{(1 + 2\alpha_K w)^2}$$

and

$$a_3 = a_3(t, z, w, \mu) = -\frac{E(t, z)}{t_*} \frac{(1 - \mu^2)(1 + 2\alpha_K w)}{s(w)}.$$

[4] Fatemi and Odeh [9]; Majorana and Pidatella [14]

Change of variables 2D [5]

In this case

$$\Phi(t,x,y,w,\mu,\phi) = s(w) f(t,x,y,w,\mu,\phi) \ ,$$

satisfies

$$\frac{\partial \Phi}{\partial t} + \frac{\partial}{\partial x}(a_1 \Phi) + \frac{\partial}{\partial y}(a_2 \Phi) +$$

$$\frac{\partial}{\partial w}(a_3 \Phi) + \frac{\partial}{\partial \mu}(a_4 \Phi) + \frac{\partial}{\partial \phi}(a_5 \Phi) = s(w)\, C(\Phi)$$

[5] Carrillo, Gamba, Majorana, Shu[6]

We choose for Si devices the value of K_* in order to have

$$\tilde{K} = 1 \quad \text{and} \quad \tilde{K}_0 = \beta \simeq 5.986,$$

and then, $t_* \simeq 3.6\, ps$ and $l_* \simeq 0.43\, \mu m$ with the numerical values given in the following table

$\hbar\omega = 0.063\, eV$
$\tilde{\alpha} = 0.5(eV)^{-1}$
$\epsilon_0 = 8.85419 \cdot 10^{-12}\, F\, m^{-1}$
$m_* = 0.32 \cdot m_0$
$D_t k = 11.4 \cdot 10^{10} eV\, m^{-1}$
$K = D_t k^2/(8\pi^2 \rho_0 \omega)$
$\alpha = 2.43694,$
$\beta = 5.986$
$n_q = 0.0958036$

$T_L = 300 K^\circ$
$\rho_0 = 2330\, Kg\, m^{-3}$
$\epsilon = 11.7 \cdot \epsilon_0$
$u_l = 9040\, m s^{-1}$
$E_{ac} = 9\, eV$
$K_0 = k_B T_L {E_{ac}}^2/(4\pi^2 \hbar {u_l}^2 \rho_0)$
$a = 11.438$
$K_* = 1.89405 \cdot 10^{-35}$

Change of variables 2D [6]

Flux terms are:

$$a_1(w,\mu) = \frac{1}{t_*}\frac{\mu s(w)}{(1+2\alpha_K w)^2}$$

$$a_2(w,\mu,\phi) = \frac{1}{t_*}\frac{\sqrt{1-\mu^2}s(w)\cos\phi}{(1+2\alpha_K w)^2}$$

$$a_3(t,x,y,w,\mu,\phi) = -\frac{1}{t_*}\frac{2s(w)}{(1+2\alpha_K w)^2} \left[E_x(t,x,y)\mu + E_y(t,x,y)\sqrt{1-\mu^2}\cos\phi\right]$$

$$a_4(t,x,y,w,\mu,\phi) = -\frac{1}{t_*}\frac{1+2\alpha_K w}{s(w)}\sqrt{1-\mu^2} \left[E_x(t,x,y)\sqrt{1-\mu^2} - E_y(t,x,y)\mu\cos\phi\right]$$

$$a_5(t,x,y,w,\mu,\phi) = \frac{E_y(t,x,y)}{t_*}\frac{\sin\phi}{\sqrt{1-\mu^2}}\frac{1+2\alpha_K w}{s(w)},$$

[6] Carrillo, Gamba, Majorana, Shu[6]

Dimensionless collision operator: Si material.

The dimensionless collision operator $C(\Phi)$ is given by

$$C(\Phi)(t,x,y,w,\mu,\phi) = G(\Phi)(t,x,y,w,\mu,\phi) - L(\Phi)(t,x,y,w,\mu,\phi)$$

Gain term

$$G(\Phi) = \frac{1}{2\pi\, t^*}\int_0^{\pi}\int_{-1}^{1} [\beta\Phi(t,z,w,\mu',\phi') + a\Phi(t,z,w+\alpha,\mu',\phi') + \Phi(t,z,w-\alpha,\mu',\phi')]d\phi' d\mu'$$

Loss term

$$L(\Phi) = \frac{1}{s(w)\, t^*}[\beta s(w) + a s(w-\alpha) + s(w+\alpha)]\Phi(t,z,w,\mu,\phi)$$

Numerical scheme

→ WENO schemes[7] to approximate by finite differences the hyperbolic fluxes using upwinding. The upwinding is component-wise and sometimes, the wind direction coincides for all points.

→ WENO flux reconstruction is used since high gradient regions appear in the evolution of the average quantities and indeed for the distribution functions. On top of this, solutions are very smooth outside the high gradient regions due to the boundary conditions and/or the doping profile.

→ Time marching algorithm until stabilization in density by 3th order RK TVD explicit method. CFL condition is guaranteed at every time step.

→ **Velocity space boundary conditions;** on w and μ ensuring that mass is preserved.

→ **Spatial Boundary conditions:** Neutral charges at contacts, transfer condition at interfaces and specular reflection at insulating walls.

- We do not need artificial cut of the w variable near 0 as in Fatemi-Odeh, WENO schemes are more reliable than higher order finite differences approximations using upwinding of Fatemi-Odeh and than finite volume kind of approximation used in Majorana-Pidatella, non parabolic band is included, we do not need implicit schemes for time evolution to stabilize oscillations (predictor-corrector schemes were used in Fatemi-Odeh[9], Majorana-Pidatella[14]).

[7] Shu[16], Lecture Notes in Mathematics, volume 1697, Springer, 1998, pp. 325-432.

MESFET Boundary conditions on $\partial\Omega = \partial\Omega_D \cup \partial\Omega_N$

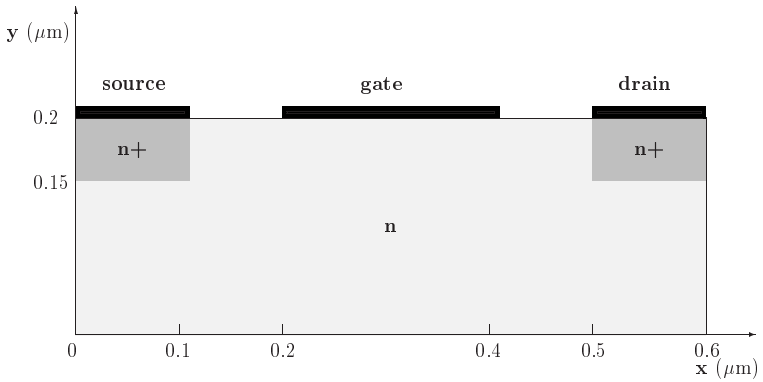

• Buffer layer of ghost points outside the MESFET domain

source and drain contacts: For $\{y = \mathbf{y}_0\}$ and $\Delta y > 0$,

$$\hat{f}(t, x, \mathbf{y}_0 + \Delta y, \mathsf{k}) = \frac{N_0}{\int_{\mathbb{R}^3} \hat{f}\, d\mathsf{k}} \hat{f}(t, x, \mathbf{y}_0, \mathsf{k}) \tag{1}$$

$\Rightarrow$ **neutral charges** at source and drain boundary regions: $\rho(t, x, \mathbf{y}_0) \approx N_0 + O(\Delta y)\, \nabla_y \rho(t, x, \mathbf{y}_0^+)$

•**Gate contact:**

$$\hat{f}(t, x, \mathbf{y}_0 + \Delta y, \mathsf{k}) = \kappa \hat{f}(t, x, \mathbf{y}_0, \mathsf{k}) \tag{2}$$

$\Rightarrow$ particles move away from the boundary forming a **depletion region** $\Rightarrow$ Robin boundary conditions

$$\nabla_y \rho(t, x, \mathbf{y}_0) \approx -\frac{\kappa}{\Delta y} \rho(t, x, \mathbf{y}_0^+). \tag{3}$$

$\Rightarrow$ **Thin Shell asymptotics**

$$\nabla_y \rho(t, x, \mathbf{y}_0) \approx E_y\, \rho(t, x, \mathbf{y}_0^+), \qquad E_y = E \cdot \eta = -\frac{\kappa}{\Delta y}, \qquad \kappa \approx \frac{\epsilon_{ox}}{2\pi\, \epsilon\, k}(V_{\text{gate}} - V) \tag{4}$$

• Insulating boundary conditions (homogeneous Neumann) on the remainder of the boundary: $\mathrm{x} \in \partial\Omega_N$

$$f(t,\mathrm{x},\mathrm{k}) = f(t,\mathrm{x},\mathrm{k}^*) \quad \text{for} \quad \mathrm{k}\cdot n(\mathrm{x}) < 0 \qquad \text{with } \mathrm{k}^* = \mathrm{k} - 2\mathrm{k}\cdot n(\mathrm{x})n(\mathrm{x}) \qquad \text{and} \quad \frac{\partial V}{\partial n}(t,\mathrm{x}) = 0.$$

Boundary conditions in velocity space

→ At $w = 0$: a "ghost point" at (w, μ) for negative w is a physical point at $(-w, -\mu)$, thus

$$\Phi_{i_1,i_2,1-j,k,l} = \Phi_{i_1,i_2,j,N_\mu+1-k,2\pi-l},\ j = 1,\ldots,3.$$

→ $\omega = \omega_{max} = N_\omega$ is taken as an outflow boundary, with a Neumann type boundary condition

$$\Phi_{i_1,i_2,N_\omega-1,k,l} = \Phi_{i_1,i_2,N_\omega,k,l}$$

and $\hat{h}_{N_\omega+1/2} = 0$ for the last numerical flux in order to enforce conservation of mass.

→ Since μ appears linearly in a_2, the numerical flux $\hat{h}_{1/2}$ in the j direction at $w = 0$ for a given μ should be the opposite of $\hat{h}_{1/2}$ in the j direction at $w = 0$ for $-\mu$ for a central scheme. To enforce conservation of mass, we average these two fluxes at $w = 0$ and use the averaged flux for both μ and $-\mu$ with opposite signs.
At $\mu = -1$ and $\mu = 1$: by the physical meaning of μ as the cosine of the angle to the z-axis,

$$\Phi_{i_1,i_2,j,1-k} = \Phi_{i_1,i_2,j,k},\ \Phi_{i_1,i_2,j,N_\mu+k} = \Phi_{i_1,i_2,j,N_\mu-k+1},\ k = 1,\ldots,3,$$

We impose $\hat{h}_0 = \hat{h}_{N_\mu+1/2} = 0$ for the first and last numerical fluxes in order to enforce conservation of mass.

$\rightarrow$ At $\phi = 0$ and $\phi = 2\pi$,for $\phi > 0$,

$$\Phi_{i_1,i_2,j,k,1-l} = \Phi_{i_1,i_2,j,k,l} \qquad \Phi_{i_1,i_2,j,k,2\pi-l} = \Phi_{i_1,i_2,j,k,2\pi+l}$$

also $\hat{h}_0 = \hat{h}_{N_\phi+1/2} = 0$ is prescribed for enforce conservation of mass.

Moments are computed by the composite mid-point rule:

$$\int_0^{+\infty} d\omega \int_{-1}^{1} d\mu \int_0^{2\pi} d\phi \; b(\omega,\mu,\phi)\Phi(t,x,y,\omega,\mu,\phi)$$

$$\approx \sum_{m=1}^{N_\phi}\sum_{l=1}^{N_\mu}\sum_{k=1}^{N_\omega} b(\omega_k,\mu_l,\phi_m)\Phi(t,x,y,\omega_k,\mu_l,\phi_m)\Delta\omega\Delta\mu\Delta\phi$$

which is at least second order accurate, (*and more accurate when Φ and its derivatives are 0 at the boundaries $\rightarrow$ further spectrally accurate for C^∞ functions with compact support.*

Setting

A uniform mesh is taken in each direction:

$$
\begin{aligned}
z_{i_b} &= (i_b - 1/2)\Delta z_b; \qquad i_b - I = 1, 2, ..., N_{z_b}, \quad b = 1, 2, \\
w_j &= (j - 1/2)\Delta w; \qquad j = 1, 2, ..., N_w, \\
\mu_k &= -1 + (k - 1/2)\Delta\mu; \qquad k = 1, 2, ..., N_\mu, \\
\phi_l &= -1 + (l - 1/2)\Delta\phi; \qquad l = 1, 2, ..., N_\phi,
\end{aligned}
$$

where $\Delta z = L/N_z$, $\Delta w = w_{max}/N_w$, $\Delta\mu = 2/N_\mu$ and $\Delta\phi = 2/N_\phi$ are the mesh sizes in each direction.

w_{max} is chosen as an integer multiple of α and Δw is chosen as $\alpha/n_{multiple}$ where $n_{multiple}$ is an integer. We avoid interpolations in the delta evaluations.

Setting

Point values of the solution $\simeq \Phi(t^n, z_i, w_j, \mu_k)$, are obtained with a dimension by dimension approximation method.

Approximation of $\frac{\partial}{\partial z}(a_1\Phi)$:

$$\frac{\partial}{\partial z}\left(a_1(w_j, \mu_k, \phi_l)\Phi(t^n, z_i, w_j, \mu_k, \phi_l)\right) \approx \frac{1}{\Delta z}\left(\hat{h}_{i+1/2} - \hat{h}_{i-1/2}\right)$$

Notice that the "wind direction" is independent of i. Without loss of generality, take $a_1(w_j, \mu_k) > 0$.

Let us denote by

$$h_i = a_1(w_j, \mu_k)\Phi(t^n, z_i, w_j, \mu_k, \phi_l), \qquad i = -2, -1, ..., N_z + 2$$

where j, k, l and n are all fixed.

WENO reconstruction[8]

We obtain the numerical flux by

$$\hat{h}_{i+1/2} = \omega_1 \hat{h}^{(1)}_{i+1/2} + \omega_2 \hat{h}^{(2)}_{i+1/2} + \omega_3 \hat{h}^{(3)}_{i+1/2}$$

where $\hat{h}^{(m)}_{i+1/2}$ are the three third order fluxes on three different stencils given by

$$\begin{aligned}
\hat{h}^{(1)}_{i+1/2} &= \frac{1}{3}h_{i-2} - \frac{7}{6}h_{i-1} + \frac{11}{6}h_i, \\
\hat{h}^{(2)}_{i+1/2} &= -\frac{1}{6}h_{i-1} + \frac{5}{6}h_i + \frac{1}{3}h_{i+1}, \\
\hat{h}^{(3)}_{i+1/2} &= \frac{1}{3}h_i + \frac{5}{6}h_{i+1} - \frac{1}{6}h_{i+2},
\end{aligned}$$

[8] Jiang and Shu [11]

WENO reconstruction 2

The nonlinear weights ω_m are given by

$$\omega_m = \frac{\tilde{\omega}_m}{\sum_{l=1}^{3} \tilde{\omega}_l}, \qquad \tilde{\omega}_l = \frac{\gamma_l}{(\varepsilon + \beta_l)^2},$$

with $\varepsilon = 10^{-6}$ and the linear weights γ_l given by

$$\gamma_1 = \frac{1}{10}, \qquad \gamma_2 = \frac{3}{5}, \qquad \gamma_3 = \frac{3}{10},$$

and the smoothness indicators β_l given by

$$\begin{aligned}
\beta_1 &= \frac{13}{12}\left(h_{i-2} - 2h_{i-1} + h_i\right)^2 + \frac{1}{4}\left(h_{i-2} - 4h_{i-1} + 3h_i\right)^2 \\
\beta_2 &= \frac{13}{12}\left(h_{i-1} - 2h_i + h_{i+1}\right)^2 + \frac{1}{4}\left(h_{i-1} - h_{i+1}\right)^2 \\
\beta_3 &= \frac{13}{12}\left(h_i - 2h_{i+1} + h_{i+2}\right)^2 + \frac{1}{4}\left(3h_i - 4h_{i+1} + h_{i+2}\right)^2 .
\end{aligned}$$

TVD $3^{rd} - order RK$

$$
\begin{aligned}
\Phi^{(1)} &= \Phi^n + \Delta t L(\Phi^n, t^n) \\
\Phi^{(2)} &= \frac{3}{4}\Phi^n + \frac{1}{4}\Phi^{(1)} + \frac{1}{4}\Delta t L(\Phi^{(1)}, t^n + \Delta t) \\
\Phi^{n+1} &= \frac{1}{3}\Phi^n + \frac{2}{3}\Phi^{(2)} + \frac{2}{3}\Delta t L(\Phi^{(2)}, t^n + \frac{1}{2}\Delta t),
\end{aligned}
$$

where L is approximated by:

$$
-\left(\frac{\partial}{\partial z_b}(a_b\Phi) + \frac{\partial}{\partial w}(a_3\Phi) + \frac{\partial}{\partial \mu}(a_4\Phi) + \frac{\partial}{\partial \phi}(a_5\Phi) + \right) + s(w)C(\Phi).
$$

TVD $3^{rd} - order RK$

Standard CFL condition for these RK schemes [9]

$$\Delta t \leq CFL \left(\frac{\Delta z_b}{max(|a_b|)} + \frac{\Delta w}{max(|a_3|)} + \frac{\Delta \mu}{max(|a_4|)} + \frac{\Delta \phi}{max(|a_5|)} \right)$$

where the maximum is taken over the grid points.

→ We take $max(|a_3|)$ over a grid without $w = 0$.

→ The source collision term is not stiff enough to change the CFL condition determined by the approximations to the spatial derivatives in our simulations.

→ Storage: In 1D three units per grid point. In a 2D solver, we use a TVD low storage third order Runge-Kutta method[10].

[9] Shu's Survey [16]

[10] Gottlieb, Shu [10]

1-D test case: n^+-n-n^+ diode short base channel diode [11]

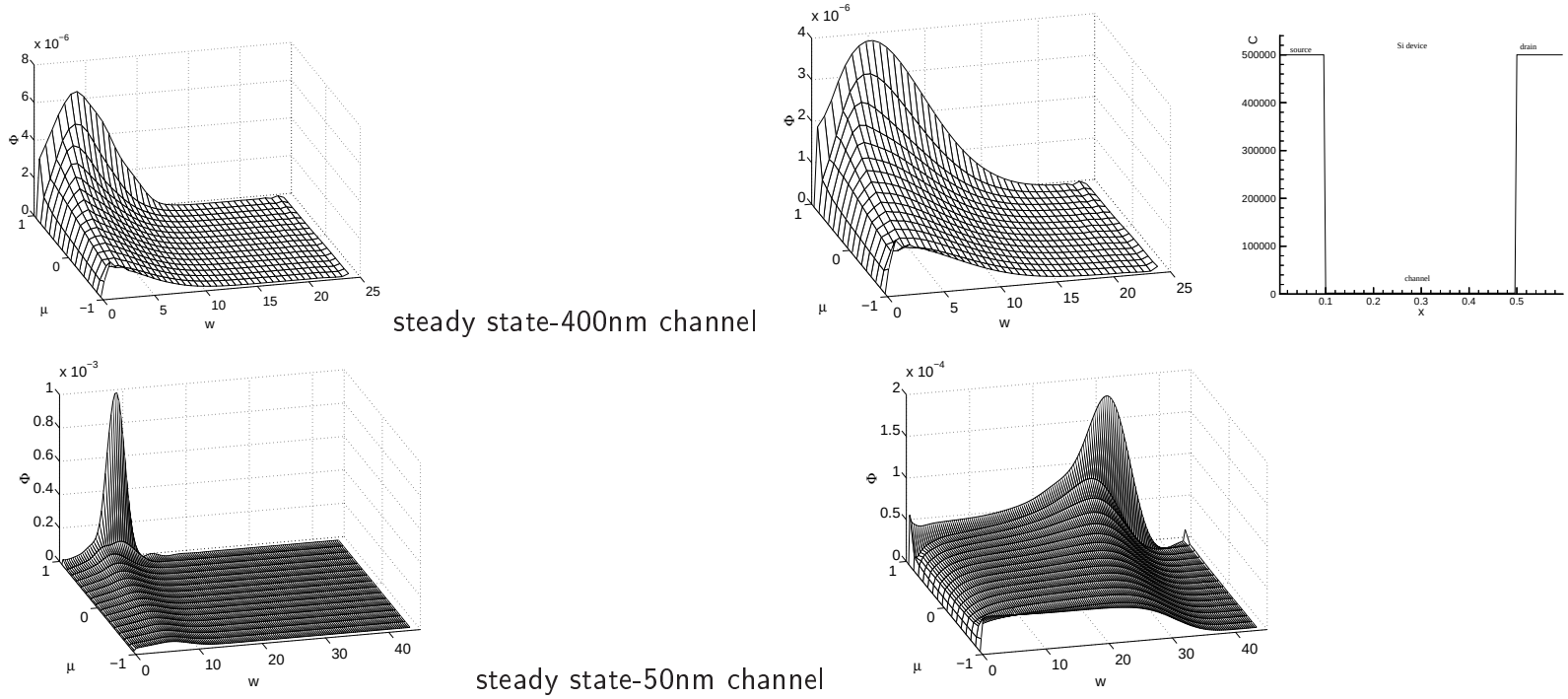

Figure 1: Spatial snapshots of the steady state transformed pdf $\Phi_\infty(z_0, w, \mu)$ for the 400 and 50 nm channel with $1V$ Vbias, at the third and forth quarters channel length

→ 400 nm channel: $N_D = 5 \times 10^{17}$ cm^{-3} in the n$^+$ region and $N_D = 2 \times 10^{15}\ cm^{-3}$ in the n region. Grid: $150 \times 40 \times 16$; $n_{multiple} = 4$. Computational time: 15 minutes.

→ 50 nm channel: $N_D = 5 \times 10^{18}$ cm^{-3} in the n$^+$ region and $N_D = 1 \times 10^{15}\ cm^{-3}$ in the n region. Grid: $150 \times 144 \times 16$; $n_{multiple} = 8$. Computational time: 30 minutes. (standard updated PC)

[11] Carrillo, Gamba, Majorana, Shu [5]

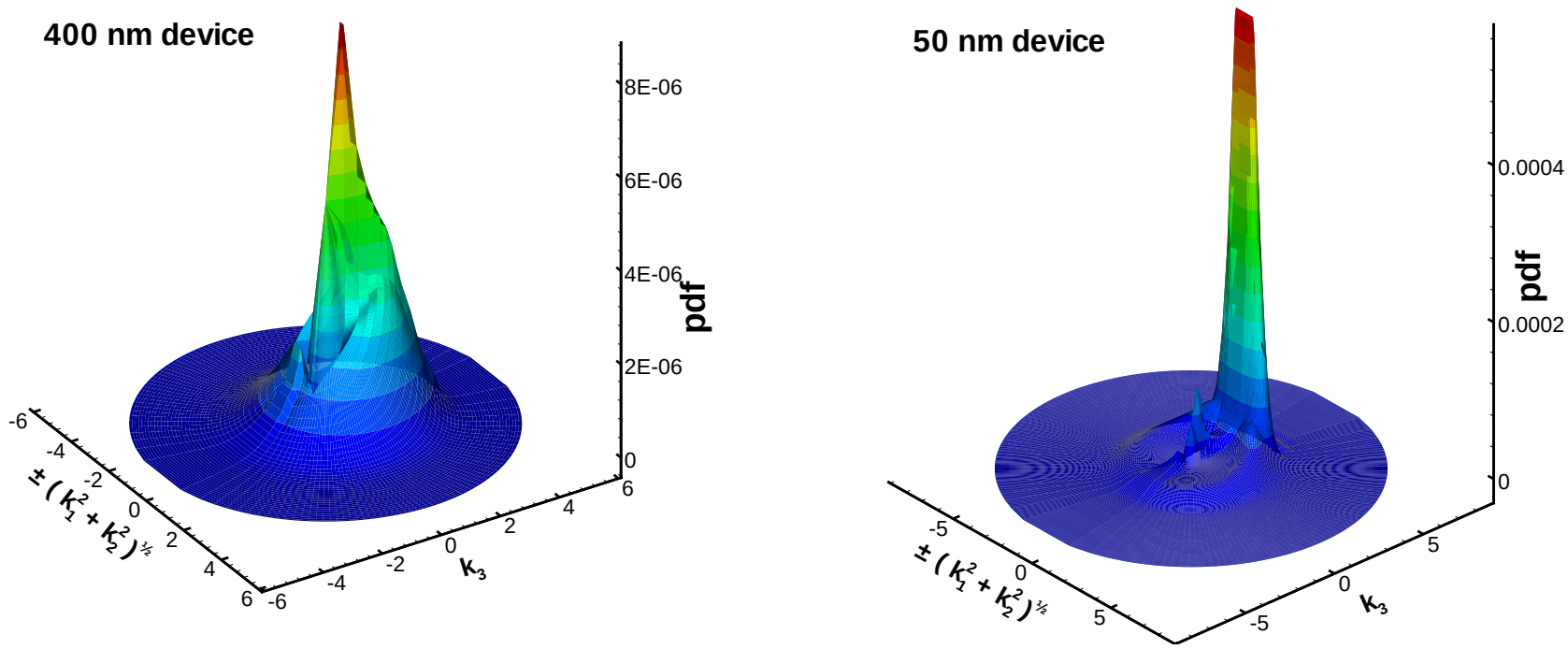

Figure 2: Pdf $F_\infty(z_0, k)$ for the 400 nm (resp. 50 nm) channel with $1V$ Vbias, in Cartesian coordinates at $z_0 = 0.5\mu m$ (resp. $z_0 = 0.125\mu m$).

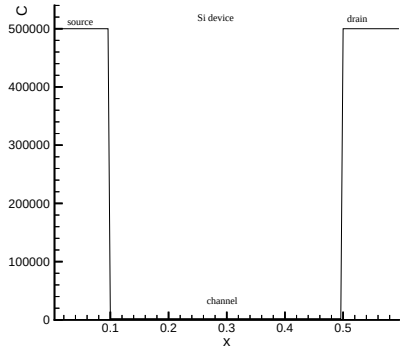

Coarse Grids 50 nm

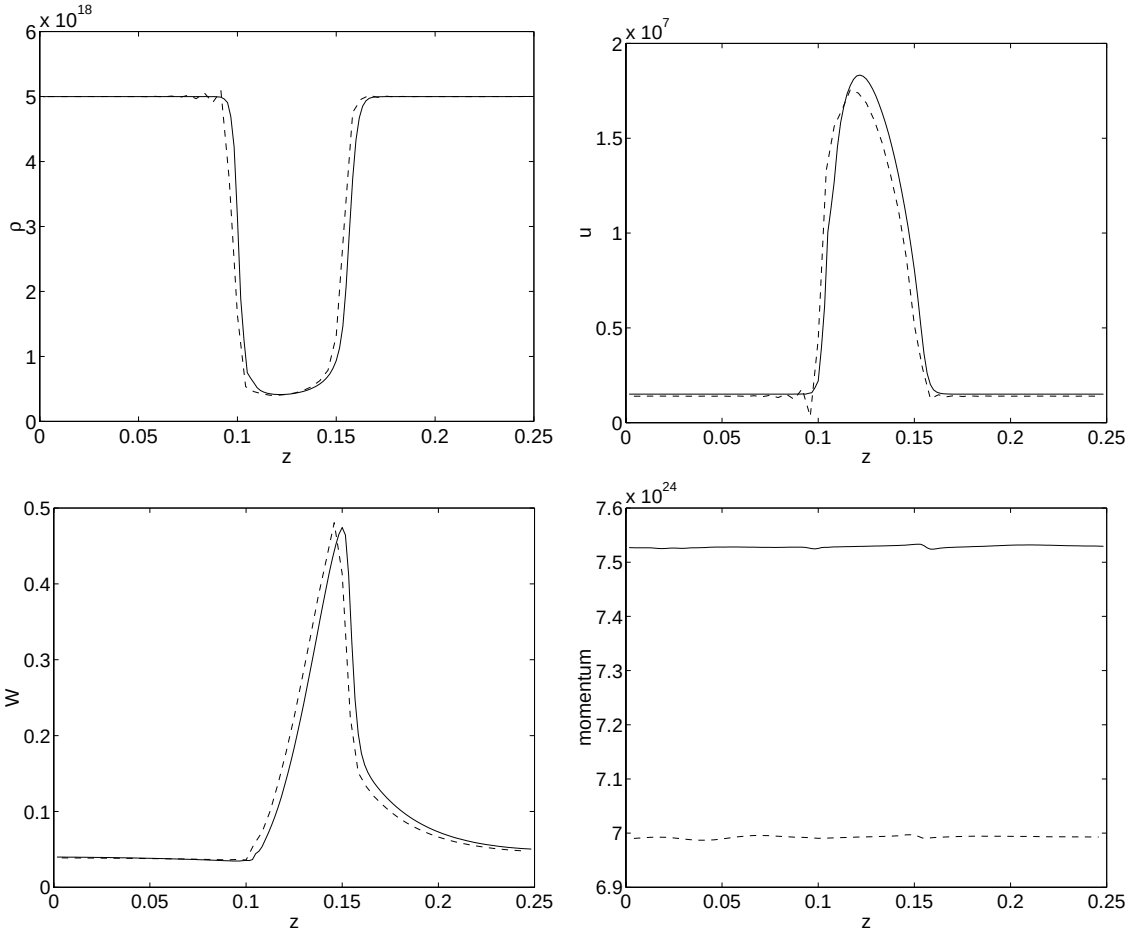

Figure 3: Comparison of macroscopic quantities for the 50 nm channel at $1V$ Vbias, between a coarse grid (dashed line) and a finer grid (solid line). Top left: density ρ in cm^{-3}; top right: mean velocity u in cm/sec; bottom left: energy W in eV; bottom right: momentum in cm^{-2} sec^{-1}.

Time evolution 50 nm

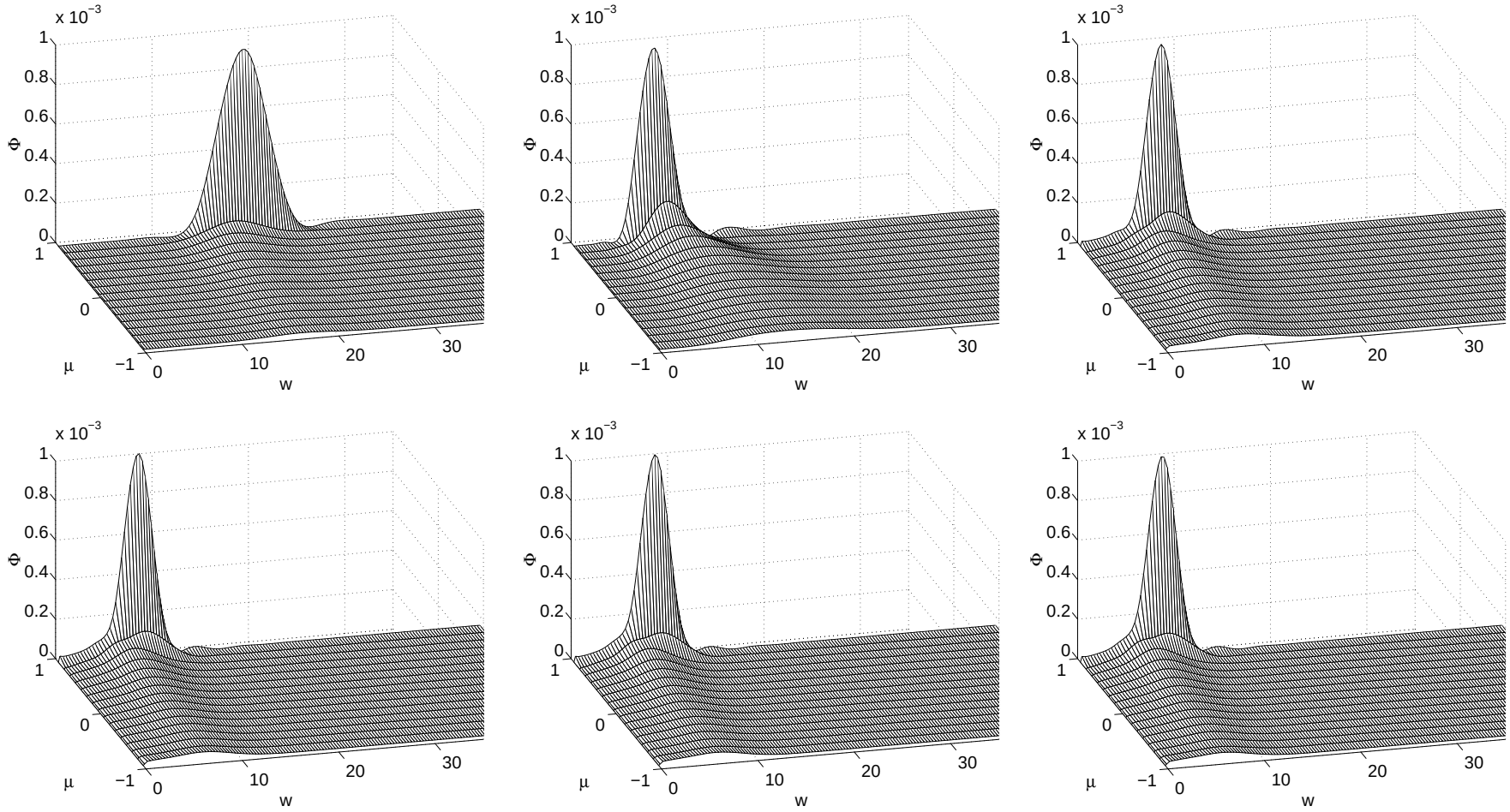

Figure 4: Time evolution of the pdf $\Phi(t_0, z_0, w, \mu)$ for the 50 nm channel with $1V$ Vbias, at $z_0 = 0.125\mu m$ from left to right and from top to bottom at times t_0=0.1, 0.2, 0.4, 0.6, 0.8 and 1.0 ps.

Time evolution
Average quantities 400 nm

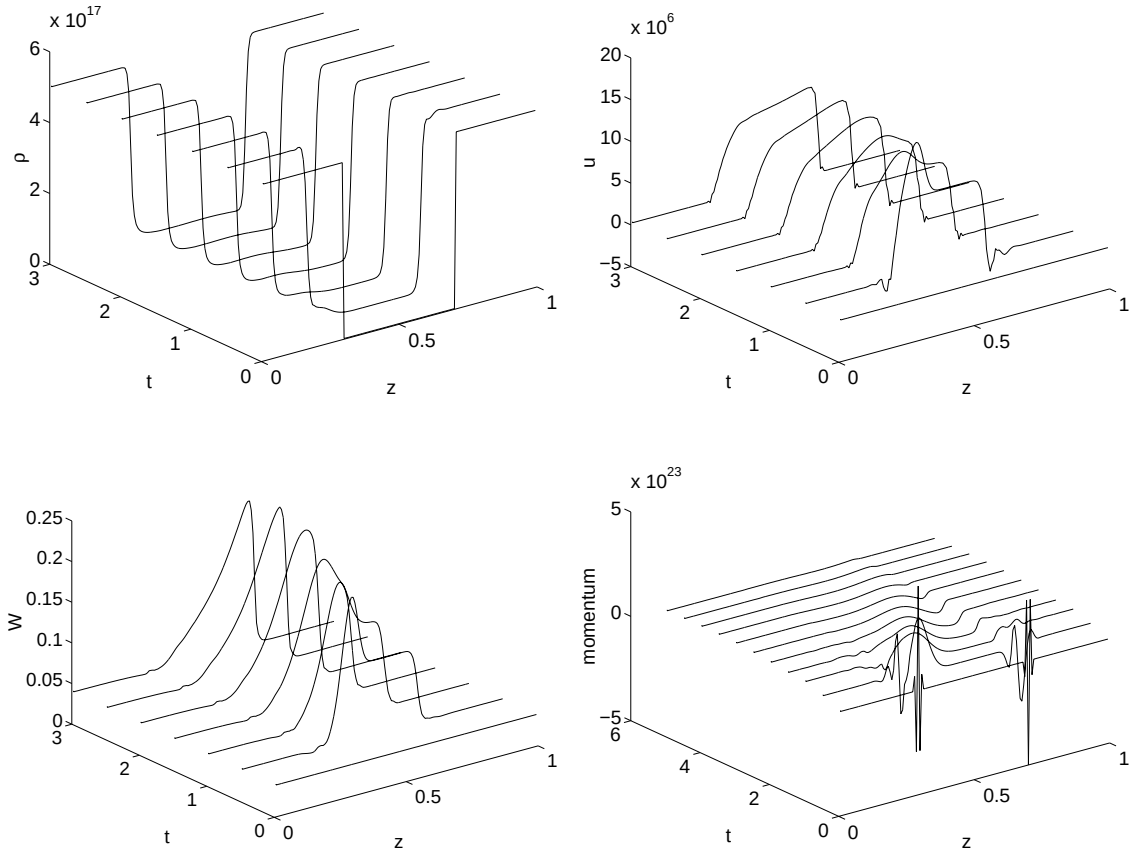

Figure 5: Evolution of macroscopic quantities for the 400 nm channel at $1V$ Vbias. Top left: density ρ in cm^{-3}; top right: mean velocity u in cm/sec; bottom left: energy W in eV; bottom right: momentum in cm^{-2} sec^{-1}.

DSMC 400 nm

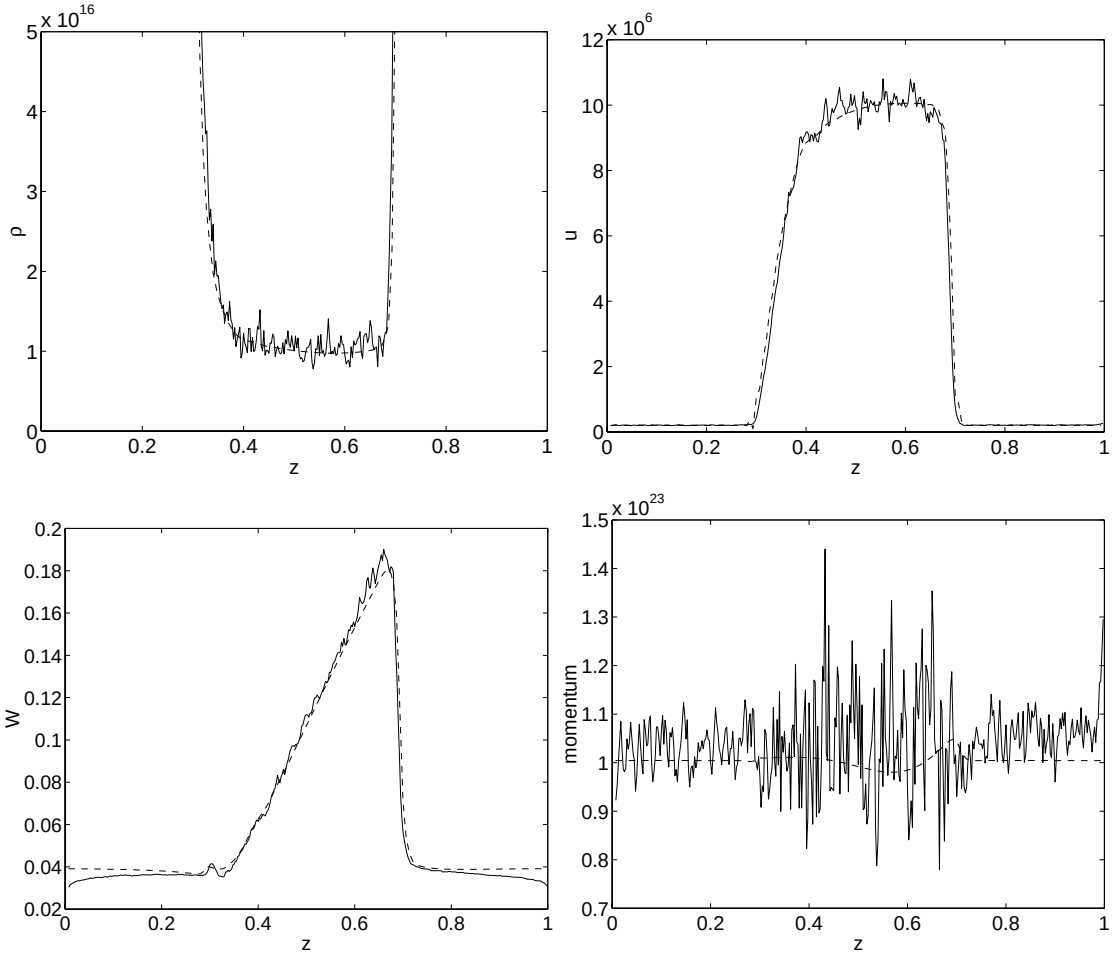

Figure 6: Comparisons for the 400 nm channel at $1V$ Vbias, between the full BP system by the DSMC method (solid line) and by the deterministic WENO solver (dashed line): top left: zoom of density ρ in cm^{-3}; top right: mean velocity u in cm/sec; bottom left: energy W in eV; bottom right: momentum in cm^{-2} sec^{-1}.

DSMC 50 nm

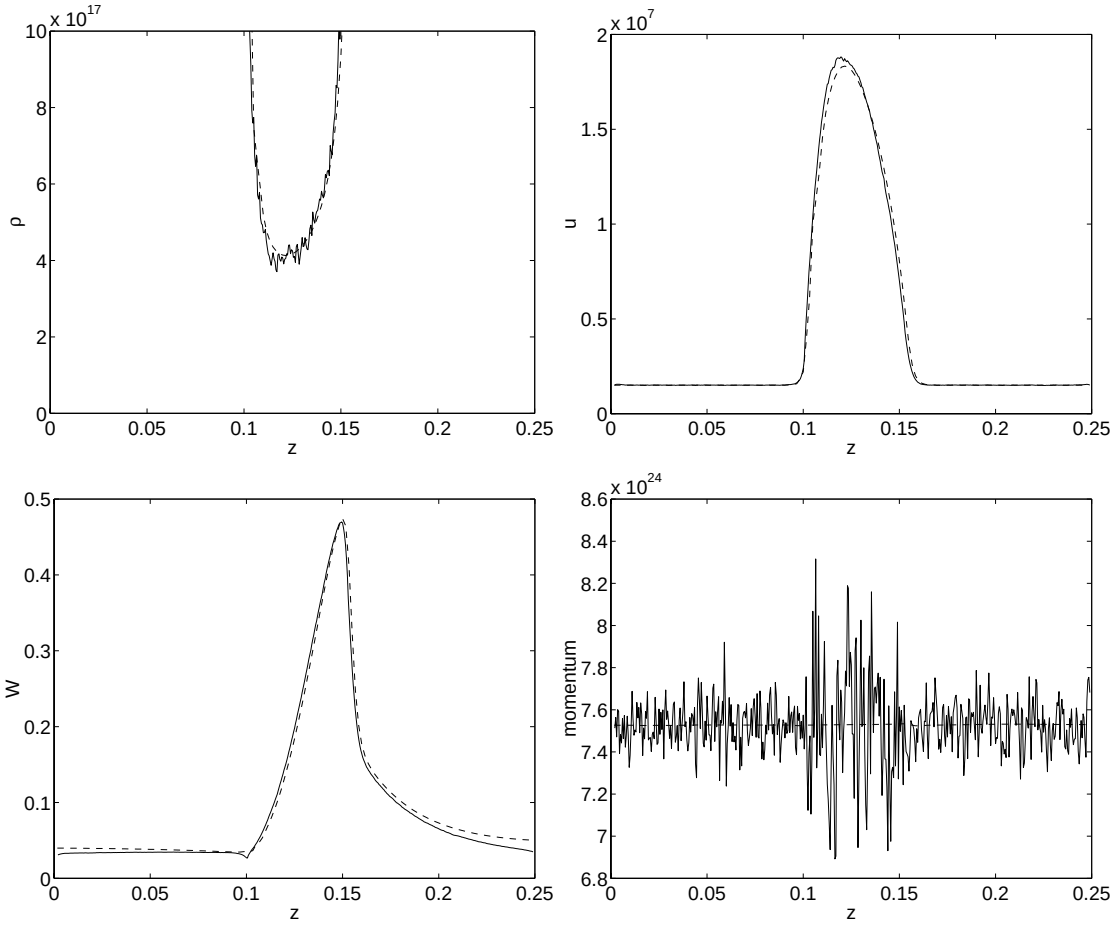

Figure 7: Comparisons for the 50 nm channel at $1V$ Vbias, between the full BP system by the DSMC method (solid line) and by the deterministic WENO solver (dashed line): top left: zoom of density ρ in cm^{-3}; top right: mean velocity u in cm/sec; bottom left: energy W in eV; bottom right: momentum in cm^{-2} sec^{-1}.

Comparisons 400 nm

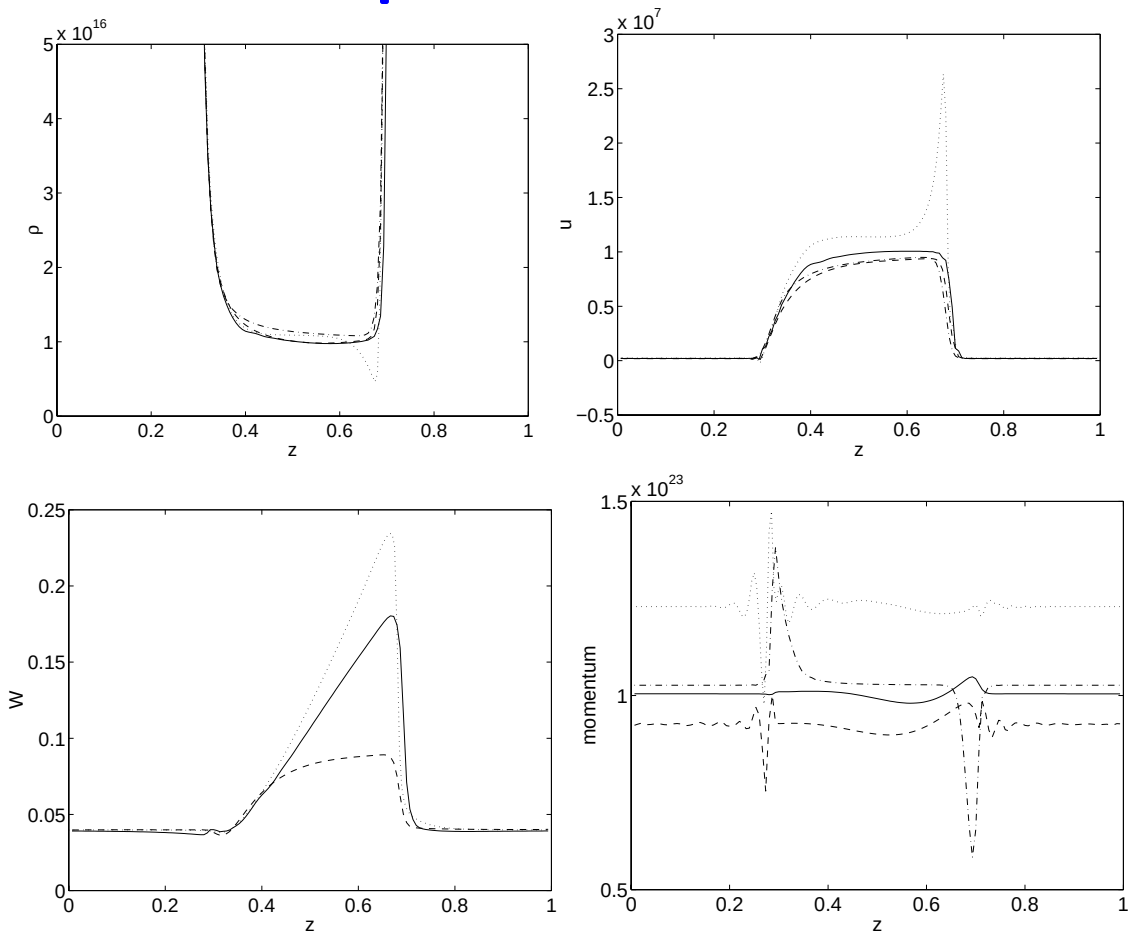

Figure 8: Comparisons for the 400 nm channel at $1V$ Vbias, between the full BP system (solid line), relaxation-time kinetic RP system (dashed line), classical hydrodynamic system HDP (dotted line) and drift-diffusion DDP system (dash-dotted line): top left: zoom of density ρ in cm^{-3}; top right: mean velocity u in cm/sec; bottom left: energy W in eV; bottom right: momentum in cm^{-2} sec^{-1}.

Comparisons 50 nm

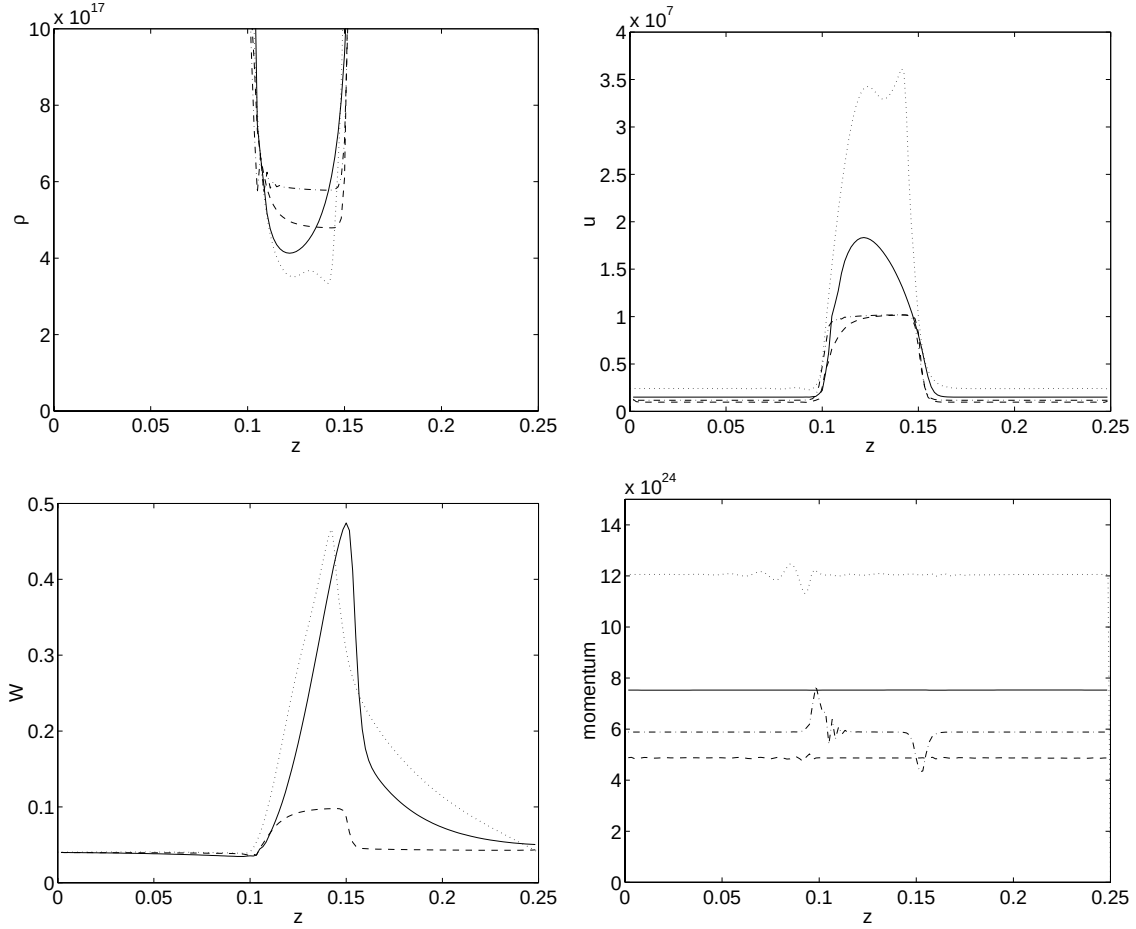

Figure 9: Comparisons for the 50 nm channel at $1V$ Vbias, between the full BP system (solid line), relaxation-time kinetic RP system (dashed line), classical hydrodynamic system HDP (dotted line) and drift-diffusion system DDP (dash-dotted line): top left: zoom of density ρ in cm^{-3}; top right: mean velocity u in cm/sec; bottom left: energy W in eV; bottom right: momentum in cm^{-2} sec^{-1}.

2-D MESFET and MOSFET Device models

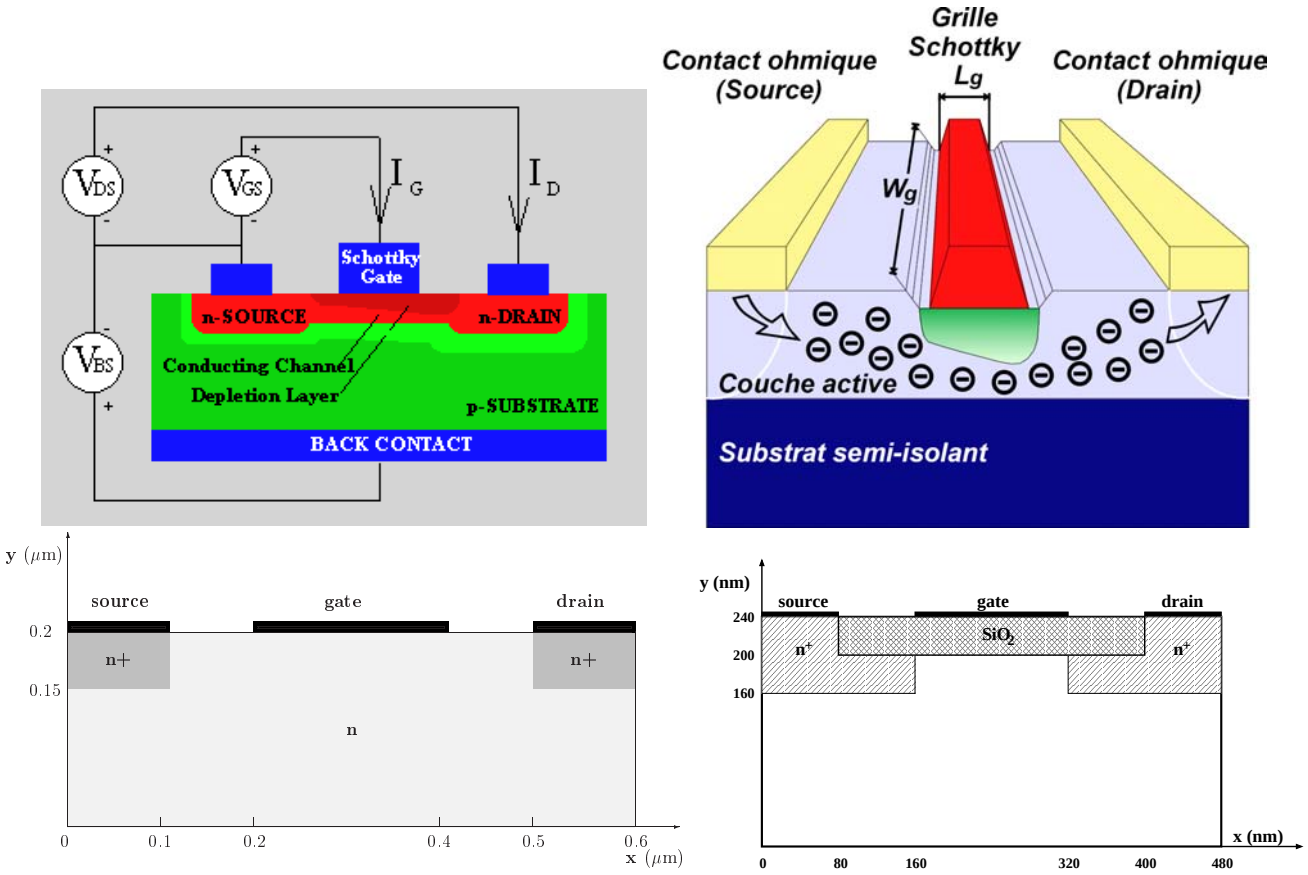

Figure 10: Schematic representation of a bidimensional MESFET

2-D MESFET and MOSFET Device models

• **2D-MESFET** geometry of the device with contact, insulating and interface boundaries generates boundaries contact singularities for the potential and blow up for electric field. $\Rightarrow$ boundary singularity formation for the mean velocity and energy, i.e. **first and second moments** of the pfd $f(\mathrm{x}_0, t, \mathrm{k})$ for x_0 the location of a jump in boundary data.

• **2D-MOSFET** geometry bounded boundary behavior for the hydrodynamic quantities

• **Grid Sizes =** $N_x \times N_x \times N_y \times N_\omega \times N_\mu \times N_\phi$ **:**

Grid A $= \mathrm{A}_{space} \times \mathrm{A}_{velocity} = 42 \times 24 \times 80 \times 12 \times 12$

Grid B $= \frac{\mathrm{GridA}}{2}$ (**coarser grid**) Grid C $= 90 \times 32 \times \mathrm{A}_{velocity}$ (**finer grid**)

• **Discrepancy error dimensionless distance between two surface:** d_j

For $q_{ij}^c =$ hydrodynamical quantity q^c at the grid point (x_i, y_j) obtained by using the coarse grid;

q_{ij}^f is the corresponding value obtained by using the fine grid.

$$d_j = \frac{1}{1+N_x} \sum_{i=0}^{N_x} d_{ij} \quad (i = 0, 1, ..., N_x)$$

$$\text{where} \qquad d_{ij} = \frac{\left| q_{ij}^c - q_{ij}^f \right|}{\max\{q^f\} - \min\{q^f\}} \quad (i = 0, 1, ..., N_x) \text{ and } (j = 0, 1, ..., N_y)$$

$N_x + 1$ and $N_y + 1$ are the #'s fine grid points in the x and y directions.

q^c is the linear interpolation at those points belonging to the fine grid but not to the coarse grid.

2-D MESFET

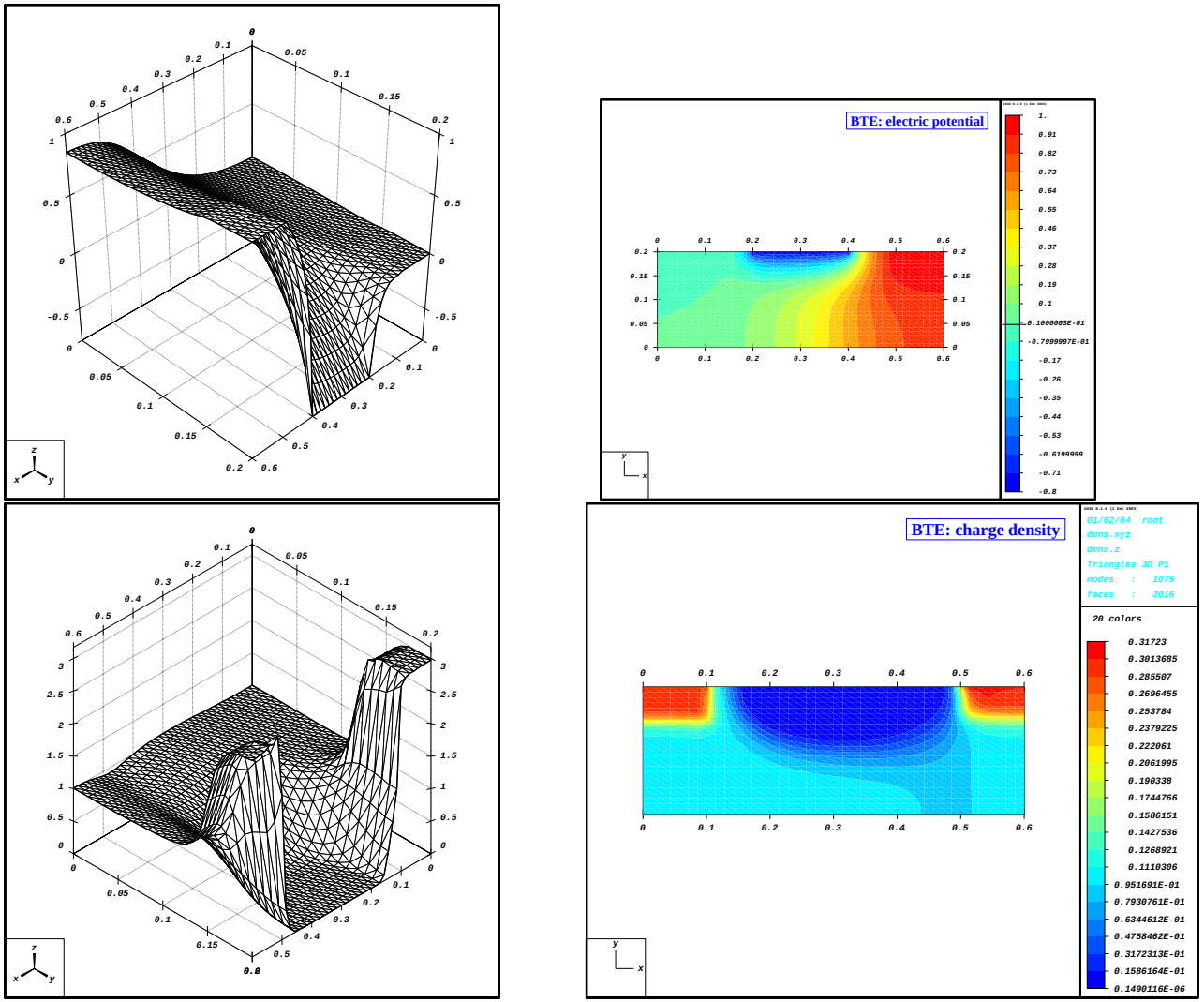

Figure 11: **Top:** Potential in V. **Botton:** Concentration in cm^{-3} - 5 ps - Grid A

2-D MESFET

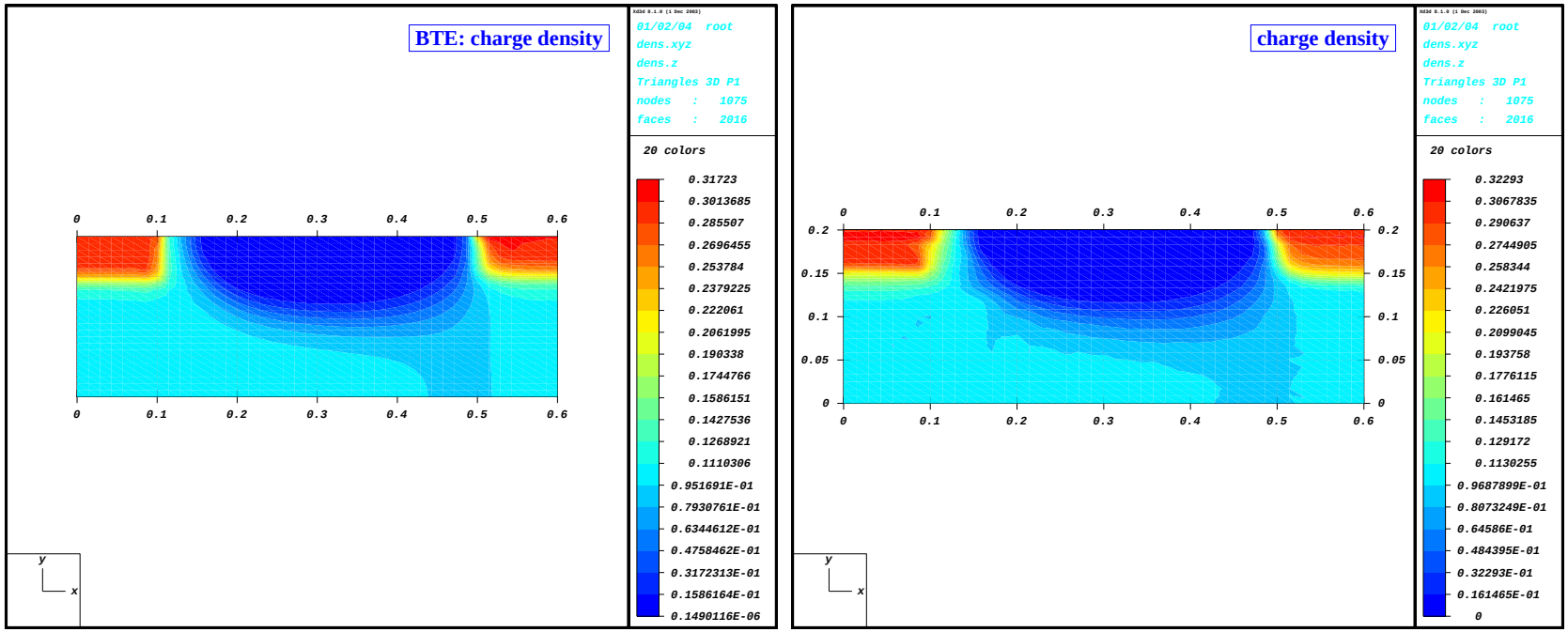

Figure 12: Comparison of concentrations BTE-MC in cm^{-3} at 5 psps - Grid A

2-D MESFET

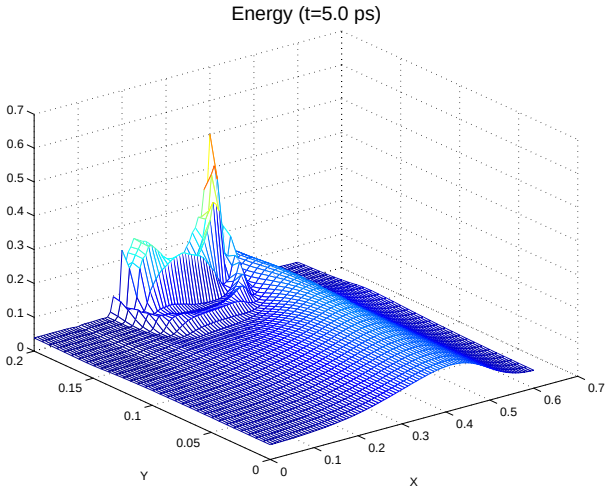

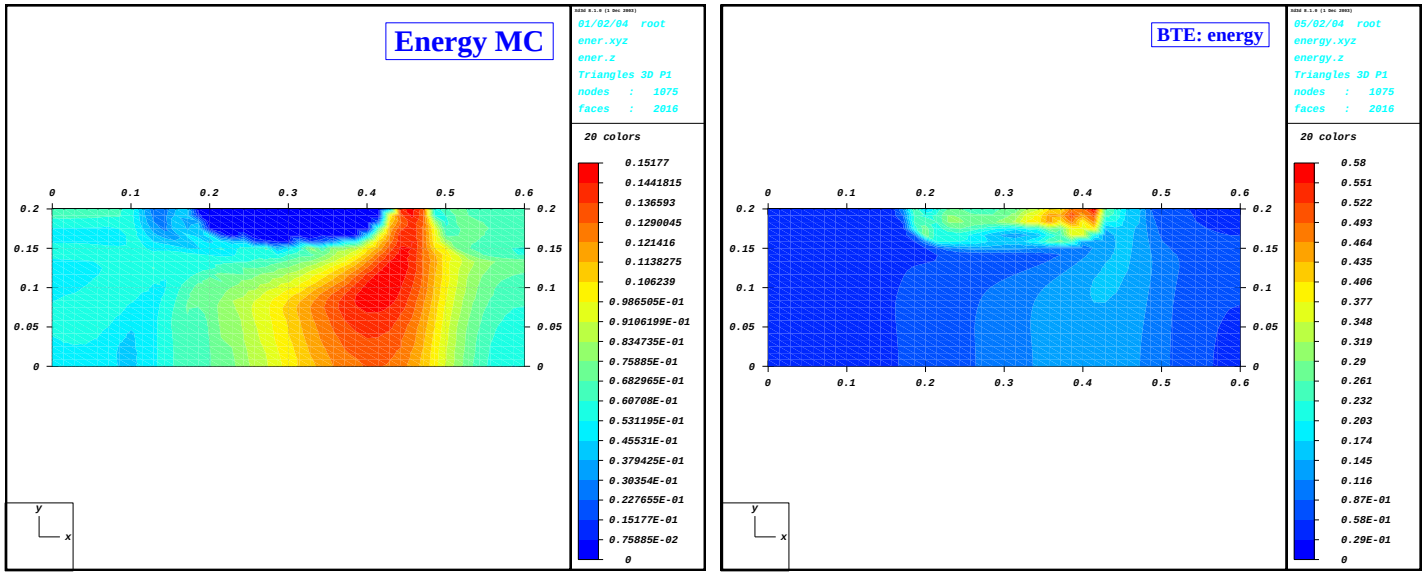

Figure 13: Energy in eV at 5 ps: comparison BTE vs MC ps - Grid A

05/02/04, 28:07, root, file: energy.xyz energy.z

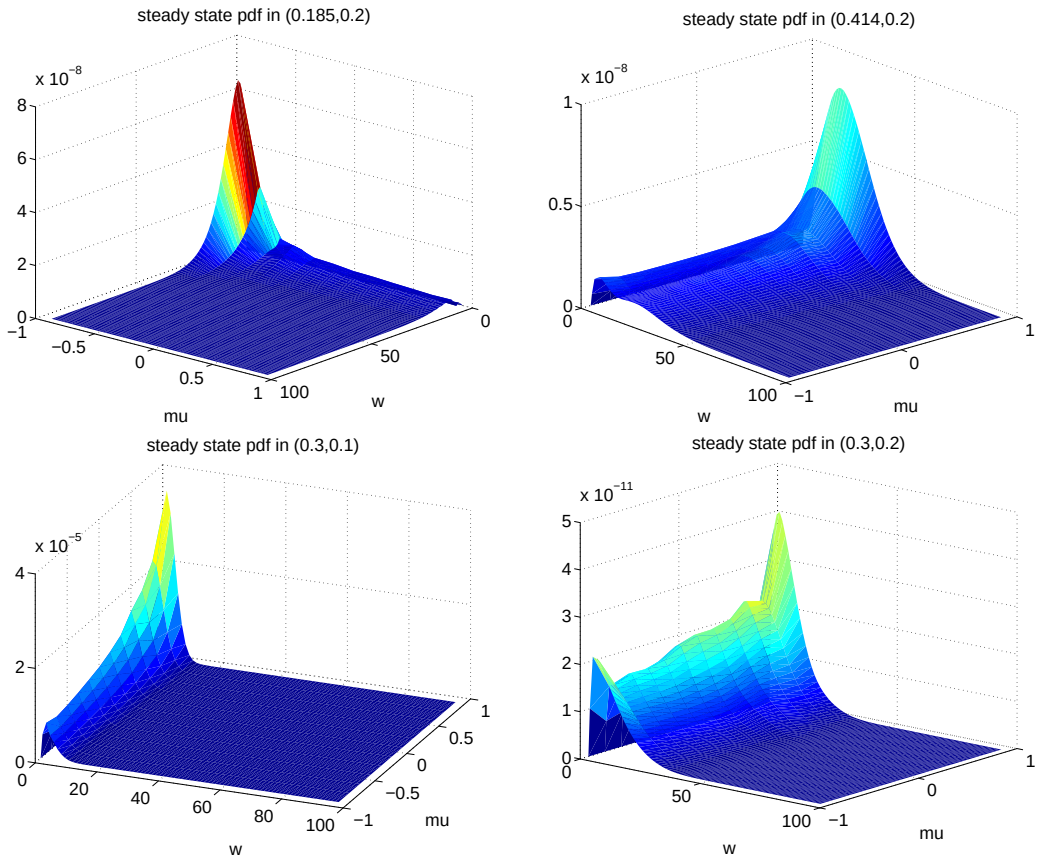

Figure 14: Steady state averaged over ϕ PDF's at different points of the MESFET for $t = 5\,ps$ - Grid A.

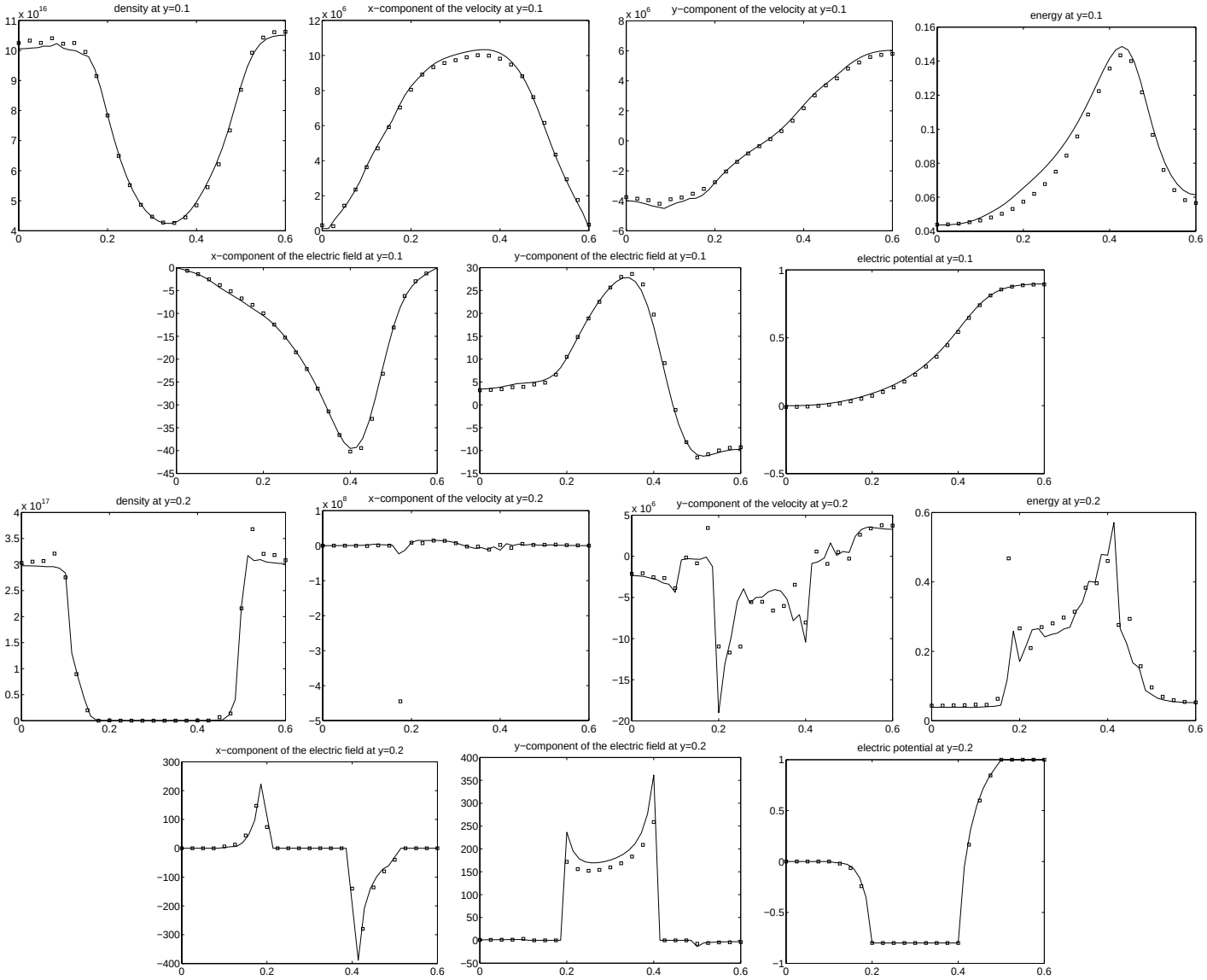

Figure 15: MESFET: Comparisons between fine and coarse grids result for BTE at 5 ps ; Solid line **Grid A** , Squares **Grid B First two top rows:** $y = 0.1$; **Lower two bottom rows:** $y = 0.2$

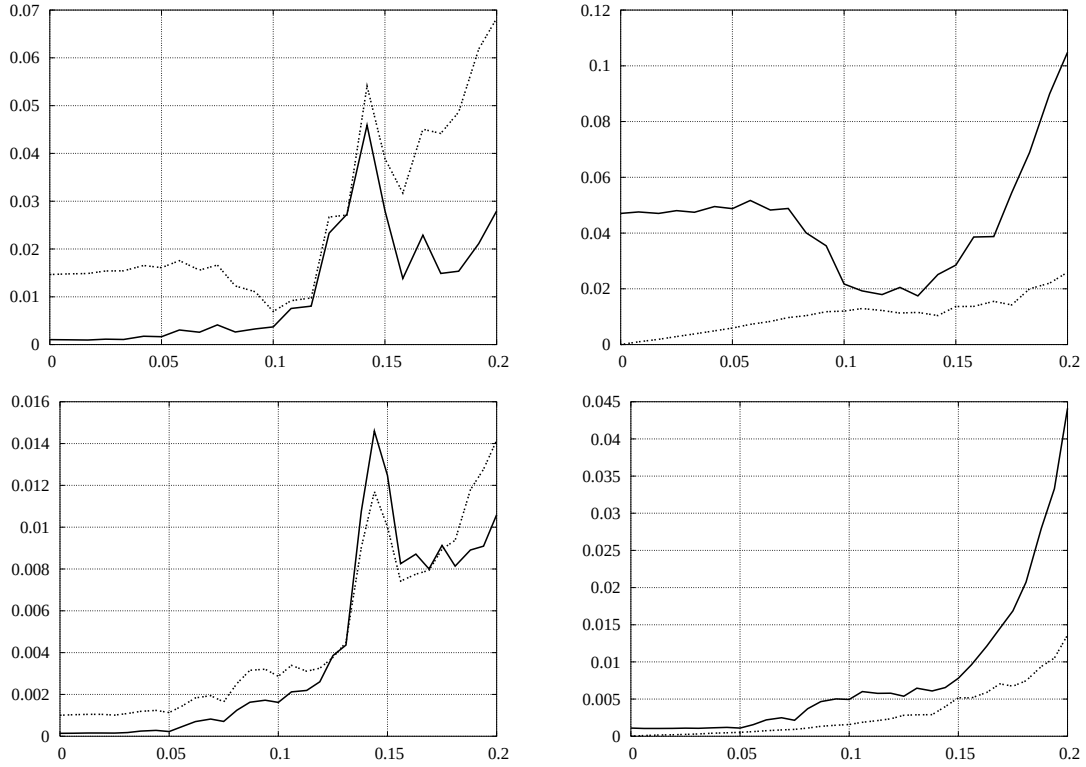

Figure 16: Dimensionless discrepancy error for fine-coarse grids at $t = 5$ps. **Top row:** Discrepancy error between grids A-B as a function of y. Left: the density ρ (continuous line) and the total energy $\rho\mathcal{E}$ (dashed line); right: the x-momentum ρu_x (continuous line) and the y-momentum ρu_y (dashed line), **Bottom row:** Discrepancy error between grids A-C as a function of y. Same as above

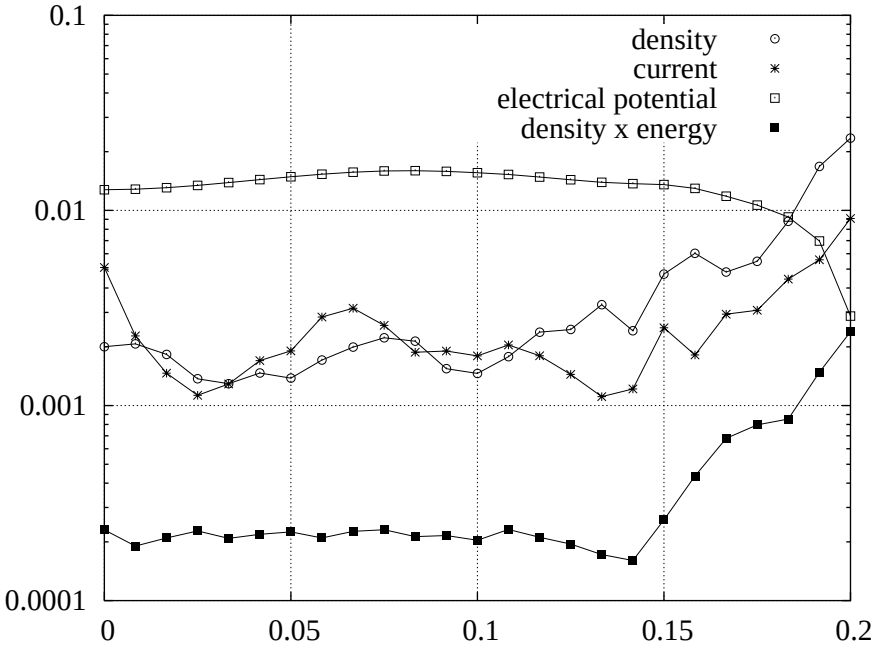

Figure 17: Average x-L^∞ difference between BTE and MC results as a function of y.

2-D MOSFET

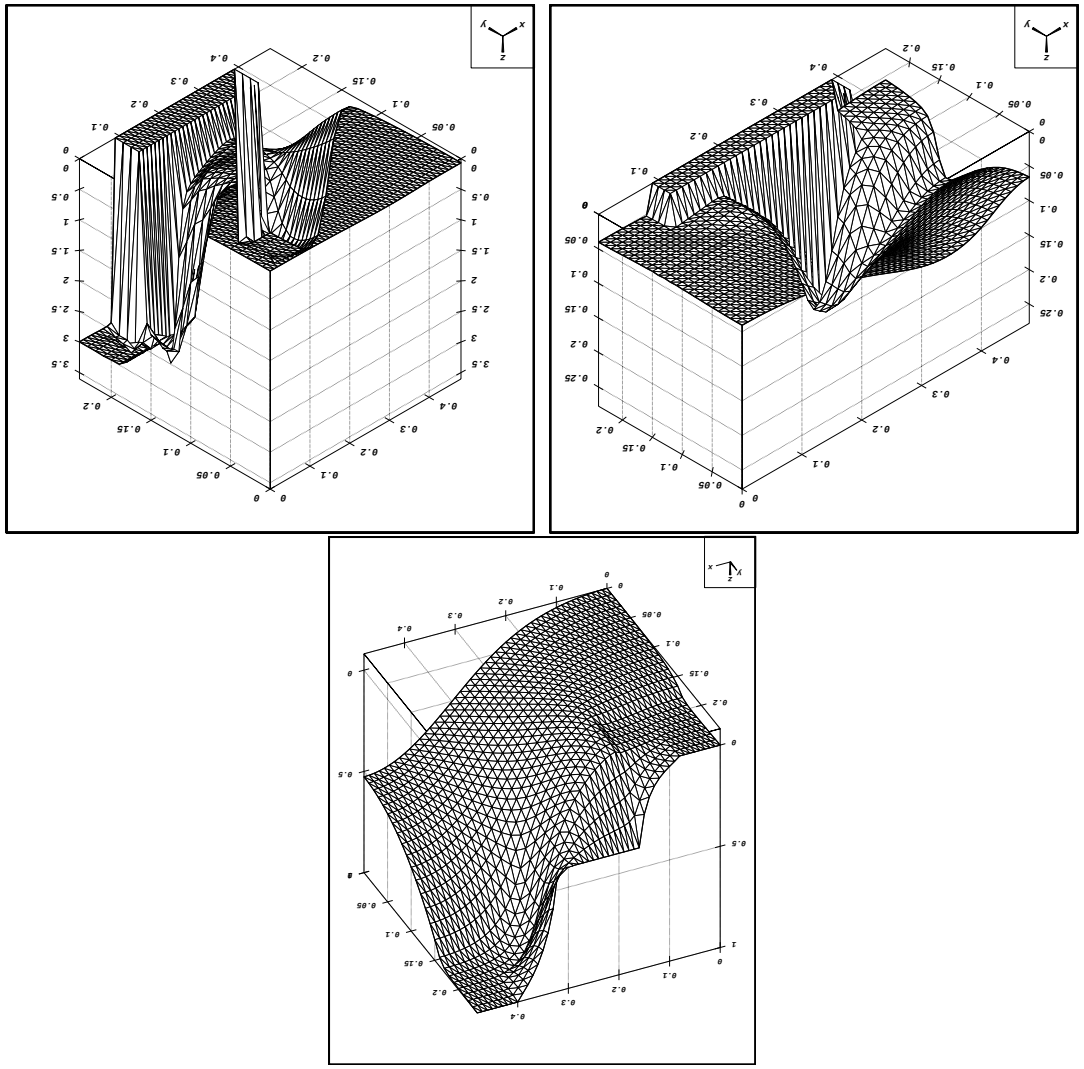

Figure 18: MOSFET device. BTE results. $t = 5$ ps. Top left: the charge density ρ $(10^{-17} \cdot cm^{-3})$; top right: the energy $\mathcal{E}$ (eV); bottom: the electric potential V.

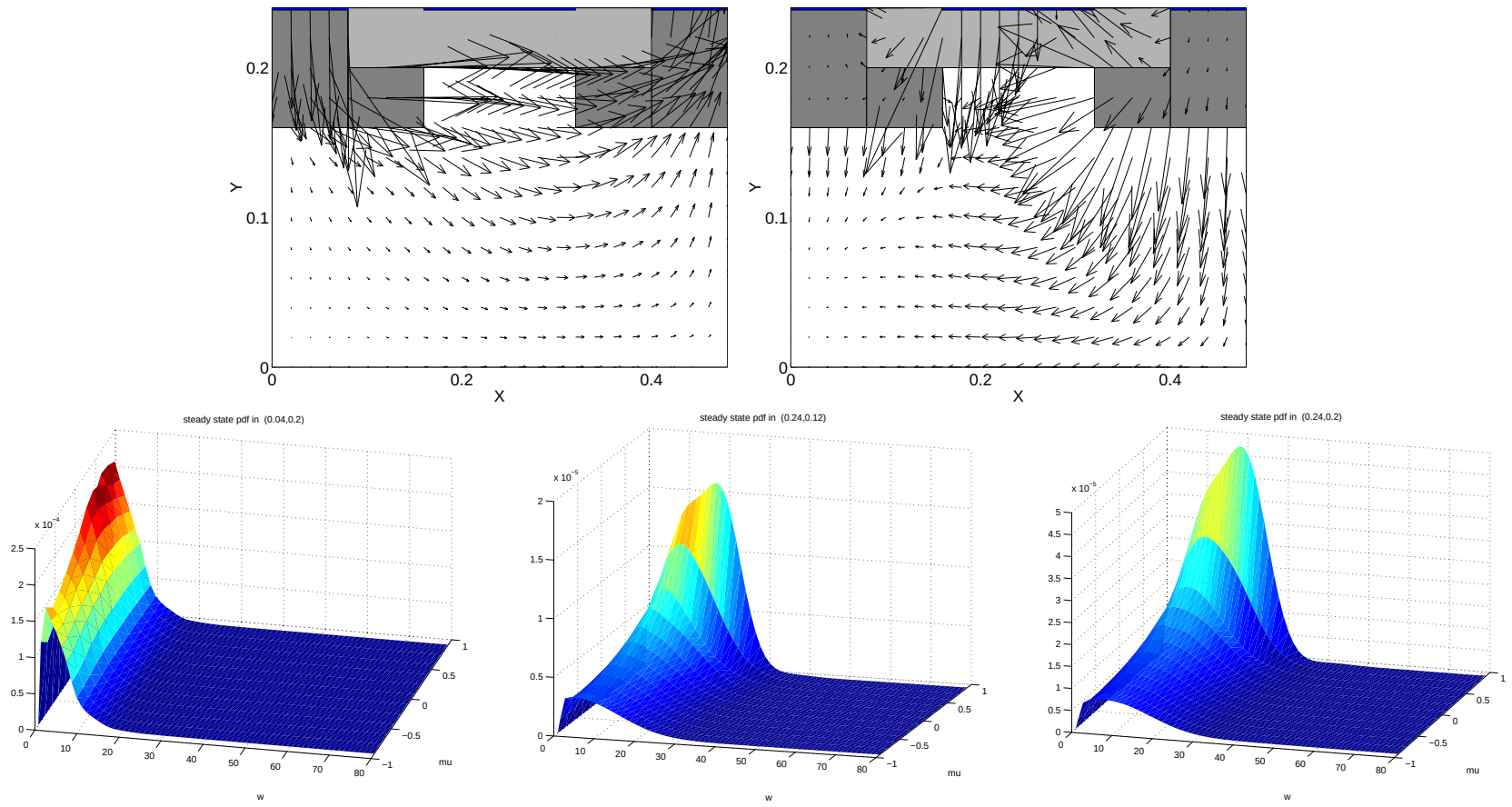

Figure 19: MOSFET - BTE results. $t = 5$ps - Grid A. **Top row:** left: the current; right: the electric field **E**. **Bottom row:** Pdf's in steady state averaged over ϕ at different locations of the MOSFET. left: at $(x, y) = (0.04, 0.2)$; center: at $(x, y) = (0.24, 0.12)$; right: at $(x, y) = (0.24, 0.2)$.

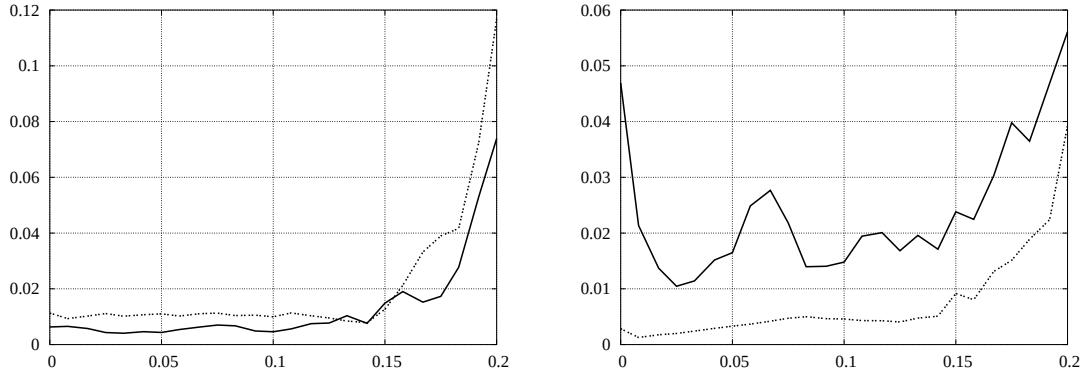

Figure 20: MESFET device. $t = 5$ ps. Discrepancies between the BTE result (grid A) and the DSMC result as a function of y. Left: the density ρ (continuous line) and the total energy $\rho\mathcal{E}$ (dashed line); right: the x-momentum ρu_x (continuous line) and the y-momentum ρu_y (dashed line).

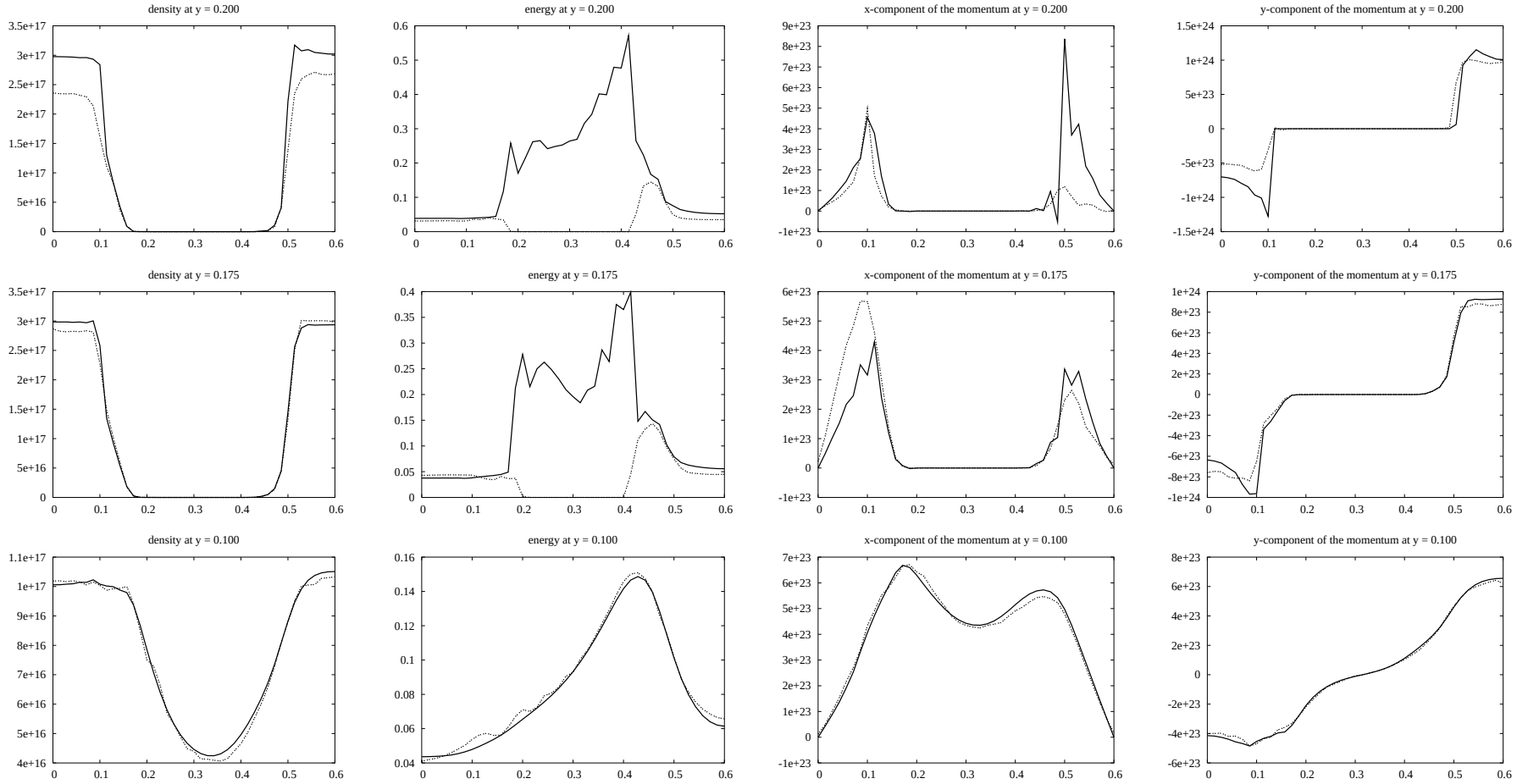

Figure 21: MESFET device. Comparisons between the BTE and the DSMC results at $t = 5$ ps. Solid line: the BTE results (grid A), dashed line: the DSMC results. left: density ρ; left middle: energy $\mathcal{E}$; right middle: the x-momentum ρu_x; secon right: the y-momentum ρu_y. **top row:** $y = 0.2$; **middle row:** $y = 0.175$; **bottom row:** $y = 0.2$.

2-D MESFET

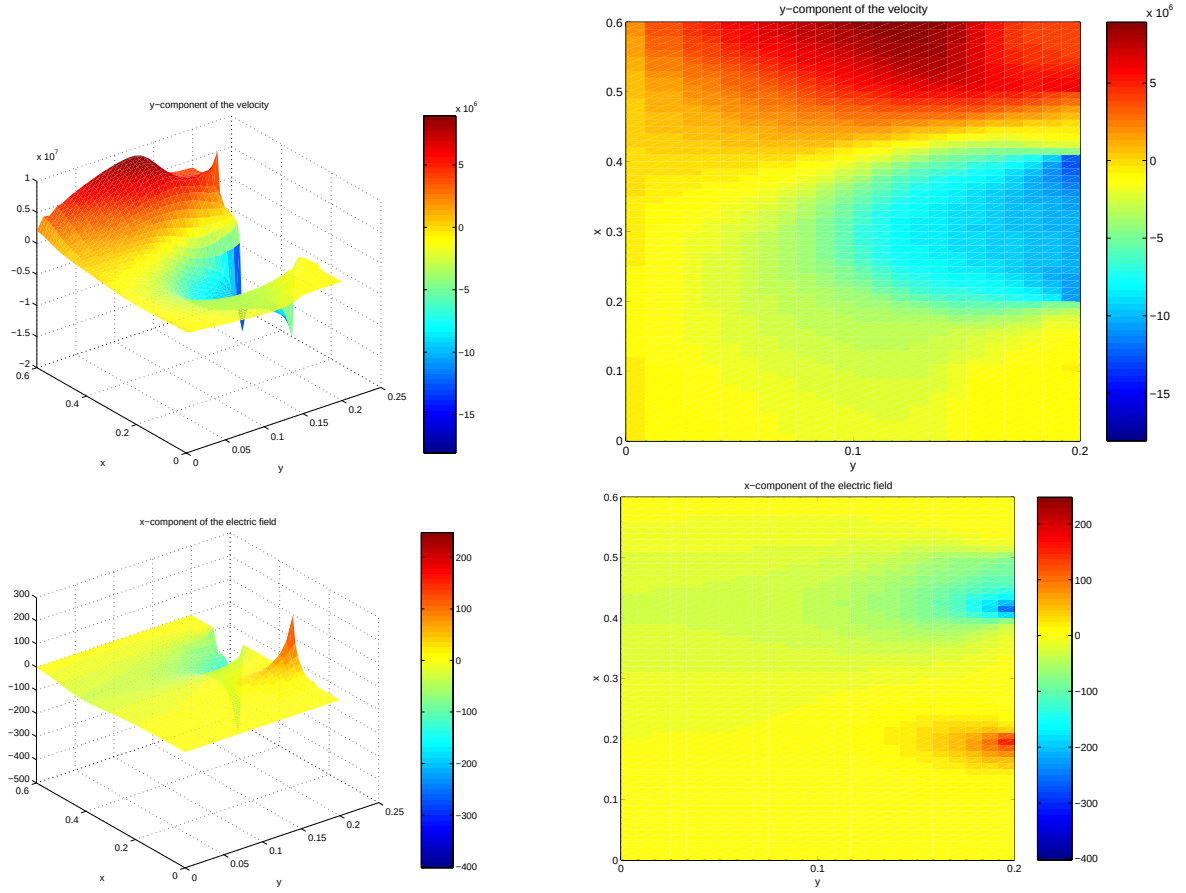

Figure 22: *Top:* x-component of mean velocity (first moment) at 5 ps. *Bottom:* left: x-component of electric field at 5 ps.

Relaxation-time model

Taking $v = \frac{\hbar k_3}{m}$. The RP approximation is given by

$$\frac{df}{dt} + v f_z - \frac{e}{m^*} E(t,z) f_v = \frac{1}{\tau}(M_{\Theta_L}\rho(f) - f)$$

with E given by Poisson equation

$$V_{zz} = \frac{\mathfrak{e}}{\epsilon}\left[\rho(t,z) - N_D(z)\right], \qquad E(t,z) = -\Psi_z.$$

M_{Θ_L} is the absolute Maxwellian given by with $\Theta_L = \frac{k_B}{m^*} T_L$.
A good approximation [12] of the mobility is

$$\frac{\mathfrak{e}}{m^*}\tau(t,x) = \frac{2\,\chi_0}{1 + \sqrt{1 + 4\left(\frac{\chi_0}{v_s} E(t,x)\right)^2}}$$

where $\chi_0 = 1400$ cm^2/V sec and $v_s = 1.03\ 10^7$ cm/sec.

[12] Carrillo, Gamba, Shu [8]; + Anile; Romano, Russo[1]

Hydrodynamical model

[13]

$$\begin{aligned}
\rho_t + (\rho u)_z &= 0 \\
(\rho u)_t + (\rho u^2 + p)_z &= -\frac{e}{m^*} E\rho - \frac{1}{\tau_m}\rho u \\
(\rho W)_t + (uW + up + q)_z &= -\frac{e}{m^*} E\rho u - \frac{1}{\tau_w}\rho(W - W_L)
\end{aligned}$$

where W is the energy density per particle

$$W = \frac{3}{2}k_B T + \frac{1}{2}m^* u^2 = \frac{3}{2}\frac{p}{\rho} + \frac{1}{2}m^* u^2,$$

p is the pressure $p = \rho k_B T$, T is the temperature and W_L is the lattice energy $W_L = \frac{3}{2}k_B T_L$. The heat flux q is assumed to satisfy Fourier's law $q = -\kappa\rho T_z$. The momentum relaxation time τ_m, energy relaxation time τ_w and heat flux coefficient κ are given by

$$\tau_m = \frac{m^* \chi_0 T_L}{\mathfrak{e} T}, \qquad \tau_w = \chi_0 T_L \left(\frac{m^*}{2\mathfrak{e}T} + \frac{3k_B T}{2\mathfrak{e}v_s^2(T + T_L)}\right) \text{ and } \kappa = \frac{3}{2}k_B^2 \frac{\tau_m T}{m^*}.$$

[13] For hydrodinamic models see [2, 3]

Conclusions

• A high order accurate finite difference weighted essentially non-oscillatory (WENO) solver for the direct numerical simulation of two dimensional Boltzmann transport equation (BTE) coupled with a Poisson equation describing two dimensional semiconductor devices, including the MESFET and MOSFET devices shows efficiency through a comparison between coarse and fine grid simulations and through a comparison with the results obtained by a direct simulation Monte Carlo (DSMC) solver.

• Clarified several issues related to the two dimensional devices including the implementation of boundary conditions, singularities, and factors important for the comparison between deterministic BTE and stochastic DSMC solvers.

• The simulation results demonstrate the superior capability of the WENO-BTE solver, which can be used to obtain accurate results with a very coarse mesh (with as few as 4 grid points in the angle directions).

Acknowledgments

Research of the first author is supported by the European IHP network "Hyperbolic and Kinetic Equations: Asymptotics, Numerics, Applications", RNT2 2001 349 and DGI-MCYT/FEDER project BFM2002-01710. Research of the second author is supported by NSF grant DMS-0204568. Research of the third author is supported by the European IHP network "Hyperbolic and Kinetic Equations: Asymptotics, Numerics, Applications" and Italian COFIN 2004. Research of the last author is supported by ARO grant W911NF-04-1-0291 and NSF grant DMS-0207451. We thank the Institute of Computational Engineering and Sciences (ICES) at the University of Texas for partially supporting this research.

We thank J.M. Mantas for many helpful comments, numerical results for grid C, discussions and figure-editing.

References

[1] Anile, A.M., Romano, V. and Russo G., "Extended hydrodynamical model of carrier transport in semiconductors", *SIAM J. Appl. Math.*, 61 (2000), pp 74-101.

[2] Baccarani, G. and Woderman, M.R., "An investigation of steady state velocity overshoot effects in Si and GaAs devices", *Solid State Electro.*, 28 (1985), pp. 407–416.

[3] Blotekjaer, K., "Transport equations for electrons in two–valley semiconductors", *IEEE Trans. on Electron Devices*, 17 (1970), pp. 38-47.

[4] J.A. Carrillo, I.M. Gamba, A. Majorana and C.-W. Shu, *2D semiconductor device simulations by WENO-Boltzmann schemes: efficiency, boundary conditions and comparison to Monte Carlo methods*, preprint (2005),to appear, `http://rene.ma.utexas.edu/users/gamba/papers/weno-opc-2d.pdf`.

[5] J.A. Carrillo, I.M. Gamba, A. Majorana and C.-W. Shu, *A WENO-solver for the 1D non-stationary Boltzmann–Poisson system for semiconductor devices*, Journal of Computational Electronics, **1**, 365–370 (2002).

[6] J.A. Carrillo, I.M. Gamba, A. Majorana and C.-W. Shu, *A WENO-solver for the transients of Boltzmann–Poisson system for semiconductor devices. Performance and comparisons with Monte Carlo methods*, Journal of Computational Physics, **184**, 498–525 (2003).

[7] J.A. Carrillo, I.M. Gamba, A. Majorana and C.-W. Shu, *A direct solver for 2D non-stationary Boltzmann-Poisson systems for semiconductor devices: a MESFET simulation by WENO-Boltzmann schemes*, Journal of Computational Electronics, **2**, 375–380 (2003).

[8] Carrillo, J.A., Gamba, I.M. and Shu, C.-W., "Computational macroscopic approximations

to the 1-D relaxation-time kinetic system for semiconductors", $Physica\ D$, 146 (2000), pp. 289–306.

[9] Fatemi, E. and Odeh, F., "Upwind finite difference solution of Boltzmann equation applied to electron transport in semiconductor devices", $J.\ Comput.\ Phys.$, 108 (1993), pp. 209–217.

[10] Gottlieb, S. and Shu, C.-W., "Total variation diminishing Runge-Kutta schemes", $Math.\ Comp.$, 67 (1998), pp. 73-85.

[11] G. Jiang and C.-W. Shu, *Efficient implementation of weighted ENO schemes*, Journal of Computational Physics, **126**, 202–228 (1996).

[12] C. Jacoboni and P. Lugli, *The Monte Carlo Method for Semiconductor Device Simulation*, Springer-Verlag, New York (1989).

[13] A. Majorana, C. Milazzo and O. Muscato, *Charge transport in 1D silicon devices via Monte Carlo simulation and Boltzmann-Poisson solver*, COMPEL, **23**, 410–425 (2004).

[14] Majorana, A. and Pidatella. R., "A finite difference scheme solving the Boltzmann-Poisson system for semiconductor devices", $J.\ Comput.\ Phys.$, 174 (2001), pp. 649-668.

[15] J.M. Mantas, J.A. Carrillo and A. Majorana, *Parallelization of WENO-Boltzmann schemes for kinetic descriptions of 2D semiconductor devices*, to appear in Mathematics for Industry Springer Series (2005). `http://kinetic.mat.uab.es/~carrillo/gallery1.html`

[16] C.-W. Shu, *Essentially non-oscillatory and weighted essentially non-oscillatory schemes for hyperbolic conservation laws*, Lecture Notes in Mathematics **1697**, 325-432 (1998).

[17] Reggiani, L., "Hot-electron transport in semiconductors", Topics in Applied Physics 58, Springer-Verlag, Berlin, 1985.